Lawrence Berkeley Laboratory
UNIVERSITY OF CALIFORNIA

Materials & Molecular Research Division

THE INFLUENCE OF CYCLIC TANGENTIAL LOADING ON INDENTATION FRACTURE

M.-C. Lu
(M.S. Thesis)

May 1984

Prepared for the U.S. Department of Energy under Contract DE-AC03-76SF00098

DISCLAIMER

LBL-17693

The Influence of Cyclic Tangential Loading on Indentation Fracture

Mei-Chien Lu

Materials and Molecular Research Division
Lawrence Berkeley Laboratory

and

Department of Materials Science and Mineral Engineering
University of California, Berkeley
Berkeley, California 94720

Master's of Science Thesis

May 1984

This work was supported by the Director, Office of Energy Research, Office of Basic Energy Sciences, Materials Sciences Division of the U.S. Department of Energy under Contract No. DE-AC03-76SF00098.

The Influence of Cyclic Tangential Loading on Indentation Fracture

Mei-Chien Lu

Materials and Molecular Research Division
Lawrence Berkeley Laboratory
and
Department of Materials Science and Mineral Engineering
University of California, Berkeley
Berkeley, California 94720

ABSTRACT

An indentation method is used to analyze the contact damage induced by cyclic tangential loading in the partial slip condition. Failure strengths are measured thereafter to indicate the degree of damage. The phenomenon of crack propagation during cyclic loading is demonstrated to occur and has been attributed to the development of residual stress fields, induced by cyclic plasticity. The principal stresses and effective shear stresses are also claculated to predict the crack geometry and the nucleation of plastic deformation. These analyses conclude that the contact damage increases as the loading ratio and the number of cycles increase.

Table of Contents

1. INTRODUCTION

1.1. General

The response of solids to indentation provides information of central interest to strength degradation by surface damage induced during contact events: particle impact, machining and subsequent erosion and wear etc.. This association is particular strong in brittle material for which indentation fracture dictates the material degradation process. The deleterious surface damage consists primarily of cracks initiated and propagated within highly localized stress fields. Classifying and analyzing the fracture patterns have been predicated on whether the contact is elastic or plastic. Elastic contact is usually analyzed by using a blunt indenter and plastic contact by a sharp indenter. The different shapes of indenters relate to the different sources of surface damage, i.e. sharp indenters to small, hard particles, and blunt indenters to contacting components. Sharp contact damage is relatively well understood. However the damage created by the contact of ceramic/ceramic components requires further attention.

The factors which determine the endurance of structural components include the geometry of the parts in contact and the condition of contact, i.e. the magnitude and direction of the contact load, the frequency of contact etc.. Furthermore, cyclic tangential loads must be involved in rotational situations, because of friction at the contact surface.

In general, failure includes both crack initiation and propagation. The dominant stage depends on the material and the loading condition. Thus, a complete analysis and understanding of both crack initiation and propagation is important and necessary.

1.2. Literature Survey

The loading of a sphere on a flat surface is just one example of a general class of contact loading systems which result in localized stress fields, otherwise known as Hertzian contact stress fields. The formation of ring cracks due to such contacts has been studied on many occasions in the presence of normal loads, and the results used in several cases to measure or define the strength and toughness. Auerbach [1] studied the critical load for production of a cone crack and Griffith [2] first put forward the idea of the existance of submicroscopic flaws. Fisher and Holloman [3] as well as Gibbs and Culter [4] have considered the strength of glass on the basis of flaw statistics. The growth of cracks was considered by Griffith to depend on the relative value of the strain energy density and the energy required to form new surfaces. Roesler [5] has shown that empirical laws seem to agree with Griffith's concepts. Furthermore, Frank and Lawn [6] investigated theoretically the development of a cone crack in the strongly inhomogeneous Hertzian stress field and discussed the path and stability of the crack. These studies constitute a second basis for understanding indentation fracture subject to normal loads.

The influence of a tangential load on indentation fracture is less well understood. The effect of sliding tractions on the stress field has been treated by Hamilton and Goodman [7], for the case of complete slip. For the same case, Lawn studied the influence of the stress field on the crack geometry as well as the effect of the friction coefficient on the critical crack formation load [8]. Later Gilroy and Hirst [9] demonstrated that the theoretical prediction of Lawn was qualitatively consistent with fracture measurements and that Auerbach's law ceases to hold when the coefficient of friction becomes relatively large.

In many practical elastic contact situations, complete slip over the contact area is prohibited by constraints on the system. Partial slip conditions then prevail. Chiang and Evans analyzed the problem of fracture initiation by coupled normal and tangential loading in the partial slip condition and found that the crack initiation load depends importantly on the magnitude of tangential force and the interfacial friction coefficient [10]. However, it remains to investigate crack propagation subject to monotonic and cyclic tangential loading in the partial slip region. The present study is concerned with an investigation of these phenomena.

1.3. Objective and Method of Approach

The present work emphasizes the effect of cyclic tangential loading on indentation fracture. For this purpose, the stress fields (both the maximum principal stress and the effective stress) due to coupled normal and tangential loading of a spherical ball on an elastic half-space are described for partial slip conditions. This analysis provides a basis for predicting the change in crack angle and in the extent of plasticity from the trends in the maximum tensile stress and shear stress with the tangential to normal load ratio. These stress fields are described in section 2.

A new experimental arrangement is designed for the study of the influence of coupled normal and tangential loads, on indentation fracture, as described in section 3. This system is utilized to examine effects of the tangential to normal load ratio, subject to cyclic tangential loading, on the critical crack formation load and the extent of crack propagation. The failure strength after indentation is also measured and the fracture surface examined by both optical and scanning electron microscopy.

All tests are conducted on glass, but the application to a wider variety of strong materials is implied. The results are described in section 4 in conjunction with a detailed discussion concerning the major and minor sources of cyclic crack growth, while the implications of the cyclic loading effect are discussed in section 5.

2. STRESS ANALYSIS

2.1. The System

A spherical indenter loaded onto a flat specimen is by far the most extensively studied elastic contact configuration by virtue of its geometric simplicity and its absence of complicating singularities. Hence, for two elastically contacting isotropic materials, subject to coupled normal and tangential loading, with superposed load cycling, the spherical indenter and semi-infinite plate are chosen as the model system.

For purposes of analysis, the two bodies are regarded as being in contact at a point, O, in the unstressed state, as shown in Fig. 1. The tangent plane of the sphere at point O then coincides with the surface plane of the semi-infinite body. Thus the tangent plane is taken as the x-y plane, and the normal to the tangent plane as the z-axis.

2.2. Stress Analysis

The foremost aim of the stress analysis is to investigate the distribution of tensile stresses, which determine the path of crack propagation [6,8]. At the same time, it is important to obtain information regarding the distribution of shear and hydrostatic stresses, which determine the extent of irreversible deformation. The formal determination of the stress field entails application of

point forces [11,12] and integration over the contact area, with the appropriate weighting functions [10]. One disadvantage of this method is that the stresses of the contact region can not be determined directly because of a singularity problem.

As background for the analysis, it is noted that the radius of the contact circle, a, under a spherical indenter, with radius R, on an elastic half-space can be expressed as [13]

$$a = \left(\frac{4}{3} k P^N R / E_1 \right)^{1/3} \tag{1}$$

where $k = \frac{9}{16}[(1-\nu_1^2)+(1-\nu_2^2)E_1/E_2]$. The coefficients ν_1, ν_2, E_1, E_2 are the Poisson's ratio and Young's modulii of the indenter and the indented materials. P^N is the magnitude of normal load, and R is the radius of the indenter. The factor k becomes unity if the indenter and indented material are of the same substance, and reduces to about 0.5 for an ideally rigid indenter. The distribution of the normal tractions across the contact surface, σ^N, is given by

$$\sigma^N = \sigma_o \left(1 - \left[\frac{r}{a} \right]^2 \right)^{1/2} \tag{2}$$

where r is the distance of any point on the surface to the center of contact, in cylindrical coordinates. The magnitude of the maximum normal pressure, σ_o, is determined by the normal load and the contact area and is given by

$$\sigma_o = \frac{3}{2} \frac{P^N}{\pi a^2} \tag{3}$$

The distribution of shear tractions induced by the tangential force, without slip, has been calculated by Mindlin [14]. This shear traction distribution for the partial slip condition is plotted in Fig. 2. The outer annular region, in which the ratio of the shear tractions to the normal tractions, $\tau_{zx}/\sigma_{zz} = f$, the friction coefficient, is the slip region and the inner circular region, with

$\tau_{zx}/\sigma_{zz} < f$, is the no-slip region[10]. These shear traction distributions are expressed in the following equations:

$$\tau_{zx} = f\sigma_o[1-(\frac{r}{a})^2]^{1/2} \qquad a^* \leq r \leq a \tag{4a}$$

$$\tau_{zx} = f\sigma_o\left\{[1-(\frac{r}{a})^2]^{1/2} - (\frac{a^*}{a})[1-(\frac{r}{a^*})^2]^{1/2}\right\} \quad 0 \leq r \leq a^* \tag{4b}$$

and

$$a^* = a[1-\frac{P^S}{fP^N}]^{1/3} \tag{4c}$$

where a^* is the radius of the no-slip region.

By assuming that the effect of elastic mismatch and the influence of tangential force to the contact area are both negligible, the surface tractions shown above are appropriate for the present system. With the known surface traction distributions, the stress field can be calculated by integration over the contact area, A_c, using the point force functions. Specifically, any component of the stress tensor beneath the surface is obtained as

$$\tau_{ij} = \int_{A_c} \tau_\alpha{}^S F_{ij\alpha}\, dA \tag{5}$$

where τ^S is the surface traction, and F is the point force function. The subscript α represents the different directions of force, N for normal and S for tangential. Hence, the stress tensor in the case of normal loading is

$$\tau_{ij} = \int_{A_c} \tau_N{}^S F_{ijN}\, dA \tag{6}$$

and the stress tensor in the case of a normal force and one tangential force is expressed by

$$\tau_{ij} = \int_{A_c} (\tau_N{}^S F_{ijN} + \tau_S{}^S F_{ijS})\, dA \tag{7}$$

The point force functions are complicated (Appendix A) and difficult to integrate analytically. A computer program is thus written (Appendix B) to obtain the stress fields, both for normal loading and coupled loading conditions. All length units used in this calculation are normalized by the radius of the contact area, a, and the stresses are normalized by the maximum normal pressure σ_o.

The tangential load is always in the positive direction and the stress distributions must be symmetric about the x-z plane. Thus, two principal stresses must lie on the x-z plane and the other is normal to it. According to Frank and Lawn [6], the normal stress is the intermediate principal stress. Hence, the maximum principal stress can be calculated by obtaining stresses in the x-z plane, as expressed by

$$\sigma_1 = \frac{(\sigma_{xx} + \sigma_{zz})}{2} + \left\{ \left[\frac{(\sigma_{xx} - \sigma_{xz})}{2} \right]^2 + \sigma_{xz}^2 \right\}^{1/2} \tag{8}$$

while the maximum principal stress, on the x-z plane, is

$$\sigma_3 = \frac{(\sigma_{xx} + \sigma_{zz})}{2} - \left\{ \left[\frac{(\sigma_{xx} - \sigma_{zz})}{2} \right]^2 + \sigma_{xz}^2 \right\}^{1/2} \tag{9}$$

The intermediate principal stress can be calculated from the hydrostatic stress p, using

$$\sigma_2 = 3p - (\sigma_1 + \sigma_3) \tag{10}$$

where $3p = (\sigma_{xx} + \sigma_{yy} + \sigma_{zz})$.

The maximum shear stress is calculated using Mises' definition of the effective stress,

$$\bar{\sigma} = \frac{1}{\sqrt{2}} \left[(\sigma_1 - \sigma_2)^2 + (\sigma_2 - \sigma_3)^2 + (\sigma_3 - \sigma_1)^2 \right]^{1/2} \tag{11}$$

or

$$\bar{\sigma} = \frac{1}{\sqrt{2}}[(\sigma_{xx} - \sigma_{yy})^2 + (\sigma_{yy} - \sigma_{zz})^2 + (\sigma_{zz} - \sigma_{xx})^2 + 6(\sigma_{xy}{}^2 + \sigma_{yz}{}^2 + \sigma_{zx}{}^2)]^{1/2} \qquad (12)$$

For present purposes, the friction coefficient is taken to be 0.3 and load ratios of 0, 0.22, 0.26 and 0.295 are used. The principal stress distributions are plotted in Figs. 3 to 6, and the maximum shear stress distributions in Figs. 7 to 10 respectively.

2.3. Maximum Tensile Stress

Comparing Figs. 3 to 6, the maximum principal stresses change substantially as the tangential force is applied. Specifically, the maximum normalized tensile stresses at the trailing edge increase as the load ratio increases and are respectively 0.163, 0.504, 0.542, and 0.573 for the above load ratios. Additionally, the area of compression beneath the contact and the tensile stresses on the surface at the leading edge diminish with increase in load ratio.

2.4. Crack Geometry

The location and orientation of crack growth generally follow the path which maximizes the energy release rate. The energy decrease caused by crack growth is expressible in terms of the integral of prior stress, multiplied by the subsequent relative displacements of corresponding points, over the crack surface. Thus, for a given system, the energy decrease at any stage of crack growth depends on the prior crack path and the prior stresses on that path. However, in the first transient of crack formation, the crack path can be predicted by the stress distribution calculated in the previous section. For isotropic materials Frank and Lawn suggested that a crack in a strongly inhomogeneous stress field would tend to follow the surface defined by the smaller principal stresses and be orthogonal to the maximum principal stress [6, 8, 15]. By examining the stress

distribution at the symmetry plane, the principal stresses σ_1 and σ_3 are in the x-z plane and σ_2 is perpendicular to the x-z plane. Thus, in accord with Frank and Lawn, the crack path can be predicted by the trajectory of σ_3 in the x-z plane. In the absence of a tangential force, the σ_3 stress trajectory (Fig. 3), from the point of maximum tensile stress, resembles a section of a fully developed cone crack, and the asymptotic angle between the σ_3 trajectory and the z-axis (68^o) is in excellent agreement with the observed cone crack angle.

In the presence of a tangential force, (Figs. 4-6) the asymptotic angle of the σ_3 trajectory at the leading edge tends to increase with increasing load ratio, while that at the trailing edge decreases. Hence, an asymmetric cone develops.

2.5. Shear Stresses

The effective shear stress distribution for a normal load condition is plotted in Fig. 7. The maximum effective shear stress occurs beneath the center of the circle of contact. Figs 8, 9 and 10 show the effect of increasing the loading ratio. The maximum effective shear stress displaces both toward the surface and the leading edge, as well as increasing in magnitude. Plastic deformation is expected to initiate from points of maximum effective shear stress, suggesting that plasticity should become more likely as the load ratio increases. Furthermore, the area inside the maximum effective shear stress contour becomes larger with increasing loading ratio. The area subject to permanent deformation should thus increase accordingly. Another interesting feature of the shear stress distribution is the small region of submaximum shear stress at the periphery of the contact area at the trailing edge. This region is susceptible to secondary plastic deformation, as discussed later.

3. EXPERIMENTAL MEASUREMENT

3.1. Specimen Preparation

Large glass plates (soda-lime glass) with pristine surfaces and 3mm in thickness were obtained and ground on one side using SiC powder (1000 grit) at the same load and period, in order to generate fine pre-existing flaws uniformly distributed on the surface. The abraded glass plates were cut into beams to obtain norminal dimensions of 0.055m×0.015m×0.003m. The cutting was effected by using a precision diamond saw in order to produce surfaces with close parallelism. Each specimen was then rounded along the edges by using 240, 400, and finally 600 grit paper to reduce the influence of edge flaws on the failure strength during subsequent bending tests.

The indenter consists of a sphere of hot pressed silicon nitride, 5mm in diameter. This selection renders the elastic constant of the indenter (E=320 GPa) to be appreciably higher than that of the indented material (E=70 GPa).

3.2. Experimental Arrangement

The indentation apparatus was designed to conduct tests at controlled levels of normal and tangential loading. As schematically shown in Fig. 11, the specimen and indenter can be placed symmetrically relative to the x-y plane, with one side in contact with a small load cell and the other in contact with a small movable steel plate, connected in series with a large screw. By rotating the screw, the steel plate can be translated and thus different loads set as needed. Both the load cell and the screw are located in a holder, mounted on a compression load cell, connected with the testing machine (MTS). A small 3mm diameter pushrod is attached to the center of the cross-head. The holder

is adjustable, therefore allowing the ball indenter to be aligned with the push-rod.

3.3. Measurement of the Coefficient of Friction

The tangential loads applied in these experiments were required to be in the partial slip region. Therefore, the coefficient of friction was measured prior to indentation testing, under conditions similar to the indentation tests.

In each test, using a fixed normal load, the specimen was arranged as shown in Fig. 11. The pushrod was translated at a constant displacement rate, causing the tangential load to increase linearly. Then, a load drop occurred immediately after the appearence of a load maximum. The maximum represents the load at which complete slip first occurs (sticking friction). For present purposes the sticking friction coefficient was determined from the ratio of the maximum tangential load to the normal load.

3.4. Cyclic Tangential Loading Tests

Reference tests were performed using only normal loads as shown in Fig. 12. Ten tests were conducted for each loading condition, in the load range from 0-300N. Then, coupled normal and tangential loading tests were performed using various fixed normal loads and varying the tangential loads to yield loading ratios of 0.22, 0.26, and 0.295 (f=0.3). Additionally, for each loading condition, cyclic tests were conducted by cycling the tangential force with a saw-tooth cycle (Fig. 13), up to 100 cycles.

To assess the influence of slow crack growth tests are also conducted at constant tangential load, with the same magnitude as the peak loads in the cyclic tests and for a period as long as the duration of the cyclic test (Fig. 14).

3.5. Crack Geometry

By examining the fracture surface of specimens failed in four-point bending tests, information regarding the angle of the crack, crack depth, and crack geometry can be obtained. Two types of fracture surface occur, shown in Figs. 15(a) and (b), which may imply different modes of damage caused by indentation.

3.5.1. Optical Microscopy

In order to obtain a general appreciation of the crack geometry, low magnification was used to examine the fracture surface. The crack depth and the distance from the boundary of the ring crack to the crack tip, projected on the surface, can be measured directively under the optical microscope and the angle of the cone crack calculated. However, this measurement is only applicable to the first type of fracture surface in which cone cracks are clearly visible.

3.5.2. Scanning Electron Microscopy

Important crack surface features develop during cyclic tangential loading. These features have to be examined at high magnification.

Hence, scanning electron microscopy was used, for both types of fracture surface.

3.6. Permanent Deformation of Surface

The plastic deformation of brittle surfaces during indentation occurs on too small a scale to be distinguished from the surface roughness of abraded surfaces. A pristine surface is thus used to ascertain the presence of permanent deformation. The deformation is identified from the surface topography

around the contact zone using both surface profilometry and interference microscopy.

4. RESULTS

4.1. Friction Coefficient

The friction coefficient is relatively variable between tests and a Weibull plot [16] is used to characterize the data (Fig. 16), obtained for a silicon nitride ball on an abraded glass surface. The most probable value of the friction coefficient is, f=0.3.

4.2. Failure Strength

The mean values of failure strength measured by four-point bending are plotted as a function of the normal load, as shown in Figs. 17, 18, and 19, where the error bars represent the standard deviation. The influence of tangential loads on the critical normal load for crack formation is shown in Fig. 17. The critical crack formation loads are obtained by extrapolating each curve to the failure strength of the original specimen. The critical crack formation load for the loading ratios of 0, 0.22, 0.26, and 0.295 are 9.8, 5.2, 4.2 and 3.7 respectively. Evidently the tangential load has a substantial effect on the critical crack formation load [10]. The failure strength are also influenced by the tangential load such that the smallest failure strength occurs for the test with the largest loading ratio. However, the major influence of the tangential load exists at the initiation stage.

The effect of cyclic loading is indicated in Fig. 18 and Fig. 19. The critical crack formation loads are not appreciably affected (for the same loading ratio), but the strengths decrease substantially as the number of cycles increases.

Furthermore, comparison of Figs. 18(a) and (b) reveals that the failure strength is much lower at the larger load ratio (Fig. 18(b)), and that the strength decreases more rapidly with cycling. Note that the magnitude of failure strength after ten cycles (with a loading ratio 0.26) approaches half the original failure strength. Cyclic tangential loading thus exists a major influence on the degree of contact damage. However, it is also noted that the rate of cyclic crack growth apparently diminishes as the number of cycles increases. This trend is evident from the failure strength determined after one hundred cycles, which is not appreciably larger than that after ten cycles. Confirmation of this trend is presented later, based on fracture surface observations.

4.3. Slow Crack Growth

A summary of the role of slow crack growth is presented in Fig. 19. In this figure, the strengths obtained after constant loading for times comparable to ten cyclic loading duration are presented in conjunction with the cyclic loading results. The relative insensitivity of the strength to the loading time (vis-a-vis the strong influence of the number of cycles) establishes that the contribution of stress corrosion cracking to crack growth is minimal.

4.4. Crack Geometry

Indentation tests conducted either with a normal load only or with one cycle of coupled loading exhibit the fracture surface depicted in Fig. 21, with evidence of a complete indentation cone crack. The cone crack angle is 68 degree [11] for normal loading and about 55 to 48 degree for coupled loading. However, for a larger number of cycles only about five percent of fracture surfaces reveal a complete cone (Fig. 21). More typically, only a small proportion of the cone appears on the fracture surface (Fig. 22). However, in all cyclic

loading cases, striations are observed on the cone crack surface near the indentation crack tip (Figs. 21-26). Furthermore, there is an exact correspondence between the number of cycles and the number of striations (Figs. 23-26). However, it is noted that the striation spacing decreases rapidly as the number of cycles increases (Fig. 29).

4.5. Permanent Deformation

The existance of permanent deformation has been established by interference micrographs and surface profilometry. Interference fringes show that a raised ridge exists outside the contact circle (Fig. 27) that extends monotonically to the original surface outside the contact zone. The change in depth of the central area, associated with the ridge, is examined using a profilometer (Fig. 28). The profilometer trace reveals that the inside zone is about 0.05μm deeper than the original surface and the ridge is about 0.15μm higher. More importantly, the leading edge is deeper than the trailing edge, even inside the contact area. This observation shows that plastic deformation [17] occurs during testing and that the extent of deformation is greater at the leading edge.

5. DISCUSSION

The two most important features of the present measurements and observations that require interpretation are firstly, the presence of cyclic load induced crack surface striations (Figs. 23-26), and secondly, the change in the fracture origin, in bending, that occurs when the indentation cracks have been formed by load cycling (Figs. 20 and 22). The striations are ostensibly similar to the fatigue striations observed in metals during cyclic crack growth. Yet, it is known from cyclic crack propagation studies that cyclic fatigue does not occur in glasses [18] (because of the absence of a crack tip plastic zone). Consequently,

the presence of striations must either derive from a cyclic manifestation of stress corrosion cracking or, alternatively, the crack driving force must increase with load cycling. The former possibility can be essentially excluded, because stress corrosion cracking would proceed most rapidly at peak load, whereas the data (Fig. 19) reveal that cycling induces substantially more crack growth.

The most plausible source of the striations, and the associated cyclic crack growth, is thus cyclic enhancement of the crack driving force. Such enhancement would not be possible in the presence of elastic loading, but can be construed upon the development of local cyclic plasticity. Indeed, the permanent distortion of the surface (Figs. 27 and 28) provides evidence to substantiate the evidence of cyclic plasticity. Local plastic deformation results in the development of residual stress, as extensively validated in studies of indentation fracture at sharp indenters [19]. The residual stress field is likely to exhibit tangential tensile stresses [20], in the elastic zone, which superpose on the elastic field depicted in Figs. 3-10. Enhanced crack growth is thus a reasonable consequence of cyclic plasticity. Furthermore, the residual stress is likely to cause a deviation in crack plane from that predicted by the elastic calculation (Figs. 3-6) in quantitative accord with present observations.

The extent of cyclic plasticity should increase as the load ratio increases, due to the corresponding increase in the maximum shear stresses (Figs. 7-10). Cycling should thus induce a large residual stress and have more extensive cyclic crack growth as the load ratio increases. This trend is entirely consistent with the present measurements (Figs. 18 and 19).

Repeated crack growth with cycling, manifest as the crack surface striations, requires explicit consideration, within the context of the plasticity induced residual stress hypothesis. Clearly, for this hypothesis to be consistent with the observations, either the extent of the plastic zone or the cyclic hardness

must increase with each cycle. Specific evidence concerning this issue has not yet been obtained. However, it is noticed that the crack growth per cycle decreases rapidly with the number of cycles (Fig. 29) indicative of an approach to crack growth saturation. Such saturation effects are commonly encountered in cyclic plasticity [21].

The change in the bend test fracture origin that occurs between normally loaded indents (from cone crack tip) and tangential, cyclically loaded indents (near contact circle) -cf. Figs. 15(a) and (b)- is also consistent with the development of plasticity induced residual stress during cycling. Specifically, fractures in bending that initiate away from the indentation crack tip and close to the contact circle must be contingent upon the existence of an appreciable near surface residual tensile stress. This requirement is in accord with plasticity induced residual stresses which exhibit their maximum tensile value at the elastic/plastic boundary viz., close to the contact circle.

Further justification for plasticity based concepts of cyclic crack growth is predicated upon consideration of the shear stresses predicted by the elastic analysis (Figs. 7-10). The maximum shear stresses for each loading condition (Tables I and II) exceed the yield strength of the glass ($\approx$3GPa estimated from hardness measurements) for all normal loads $>$ 80N, especially at larger load ratios. Again, therefore, the existence of plasticity appears plausible. Furthermore, tangential loads are expected to produce enhance deformation at the leading edge, consistent with the larger surface depression at this edge determined from the profilometer trace (Fig. 28).

Finally, some additional remarks are presented regarding the exclusion of cyclic crack propagation, in the metallurgical context, as the source of crack surface striations. The fatigue striation spacing Δs is known to increase with the stress intensity amplitude ΔK, for all metallic materials, as [22]

$$\Delta s \approx 6(\Delta K/E)^2 \qquad [13]$$

A plot of the striation spacing determined from Fig. 25 with ΔK estimated using the indentation approximation for large cracks [23],

$$K \approx P/c^{3/2} \qquad [14]$$

where P is the indentation load and c is the crack depth, reveals (Fig. 30) that Δs decreases less rapidly with ΔK ($\Delta s \propto \Delta K^{0.8}$) than typically encountered during fatigue crack growth ($\Delta s \propto \Delta K^2$). The existance of an alternative mechanism of cyclic crack growth is thus, again, suggested.

6. CONCLUDING REMARKS

Several features of the present work specifically add to the current understanding of the indentation fracture problem. Firstly, a stress analysis, based upon principal and shear stresses indicates that the tensile stresses are increased at trailing edge by the application of tangential forces, such that the critical crack formation load decreases and the crack angle increases at this edge. Consequently, the failure strength decreases as the tangential force increases. In addition, the shear strength increases, allowing the specimens to deform plastically more readily, especially at the leading edge.

The second feature of this analysis is the concept that residual stresses, induced by the plastic deformation at the contact area, constitute the driving force for crack propagation during cyclic loading. The deformation is deemed to be cumulative, causing the failure strength to decrease as the number of cycles increases. However, the crack growth per cycle decreases with number of cycles and tends to saturate at an effective endurance limit.

Acknowledgement

I would like to thank Prof. A.G. Evans for his guidance and support during this work. The assistance received from the wokers in ceramic lab are also appreciated. They are indebted to D.B. Marshall and Peter Ruegg for the assistance with experimental design, to Chun-Hway Hsueh and Shu-Sheng Chiang for theoretical aspects of the problem. Helpful conversations and correspondence with others are also gratefully acknowledged.

Finallly, I thank my parents, my brother and sisters for their love, understanding and encouragement through these years.

This work was supported by the Director, Office of Energy Research, Office of Basic Energy Sciences, Materials Sciences Division of the U.S. Department of Energy under Contract No. DE-AC03-76SF00098.

APPENDIX A

Point force functions which describe the stress fields created by unit normal load (expressed by h_{ij} for each component) or unit tangential load (expressed by g_{ij}), on a semi-infinite elastic homogeneous solid, bounded by the plane $z = 0$, are shown in Fig. 31. These functions are listed in the following equations :

$$h_{xx} = \frac{1}{2}\pi\left\{\frac{(1-2\nu)z}{R^3} - \frac{3x^2z}{R^5} - \frac{(1-2\nu)}{R(R+z)}\left[1 - \frac{x^2}{R(R+z)} - \frac{x^2}{R^2}\right]\right\}$$

$$h_{yy} = \frac{1}{2}\pi\left\{\frac{(1-2\nu)z}{R^3} - \frac{3y^2z}{R^5} - \frac{(1-2\nu)}{R(R+z)}\left[1 - \frac{y^2}{R(R+z)} - \frac{y^2}{R^2}\right]\right\}$$

$$h_{zz} = \frac{-3z^3}{2\pi R^5}$$

$$h_{yz} = \frac{-3yz^2}{2\pi R^5}$$

$$h_{zx} = \frac{-3xz^2}{2\pi R^5}$$

$$h_{xy} = \left[\frac{-3xyz}{R^5} + \frac{(1-2\nu)(2R+z)xy}{R^3(R+z)^2}\right]$$

$$g_{xx} = \frac{x}{2\pi}\left\{\frac{1-2\nu}{R^3} - \frac{3x^2}{R^5} - \frac{(1-2\nu)}{R(R+z)^2}\left[3 - \frac{x^2(3R+z)}{R^2(R+z)}\right]\right\}$$

$$g_{yy} = \frac{x}{2\pi}\left\{\frac{1-2\nu}{R^3} - \frac{3y^2}{R^5} - \frac{(1-2\nu)}{R(R+z)^2}\left[1 - \frac{y^2(3R+z)}{R^2(R+z)}\right]\right\}$$

$$g_{zz} = \frac{-3xz^2}{2\pi R^5}$$

$$g_{yz} = \frac{-3xyz}{2\pi R^5}$$

$$g_{xz} = \frac{-3x^2z}{2\pi R^5}$$

$$g_{xy} = \frac{y}{2\pi}\left\{\frac{-3x^2}{R^5} - \frac{(1-2\nu)}{R(R+z)^2}\left[1 - \frac{x^2(3R+z)}{R^2(R+z)}\right]\right\}$$

where $R = (x^2 + y^2 + z^2)^{1/2}$.

APPENDIX B

The integration routine described here is written to calculate the stress distribution beneath the surface. These coordinate and dummy variables used in this program are shown schematically in Fig. 31.

```
 hxx(x2,z,R,R2,R3,R5,Rz)=1./6.2823*(0.5*z/R3-3*x2*z/R5-0.5/R/Rz*(1.
&-x2/R/Rz-x2/R2))
 hyy(y2,z,R,R2,R3,R5,Rz)=1./6.2823*(0.5*z/R3-3*y2*z/R5-0.5/R/Rz*(1.
&-y2/R/Rz-y2/R2))
 hzz(z3,R5)=1./6.2823*(-3)*z3/R5
 hyz(y,z2,R5)=1./6.2823*(-3)*y*z2/R5
 hxz(x,z2,R5)=1./6.2823*(-3)*x*z2/R5
 hxy(x,y,z,R,R3,R5,Rz)=1./6.2823*((-3)*x*y*z/R5+0.5*x*y*(2*R+z)/R3/
&Rz**2)
 gxx(x,x2,z,R,R3,R5,Rz)=1./6.2823*x*(0.5/R3-3*x2/R5-0.5/R/Rz**2*(3.
&-x2*(3*R+z)/R**2/Rz))
 gyy(x,y2,z,R,R2,R3,R5,Rz)=1./6.2823*x*(0.5/R3-3*y2/R5-0.5/R/Rz**2*
&(1.-y2*(3*R+z)/R2/Rz))
 gzz(x,z2,R5)=1./6.2823*(-3)*x*z2/R5
 gyz(x,y,z,R5)=1./6.2823*(-3)*x*y*z/R5
 gxz(x2,z,R5)=1./6.2823*(-3)*x2*z/R5
 gxy(y,x2,z,R,R2,R5,Rz)=1./6.2823*y*((-3)*x2/R5-0.5/R/Rz**2*(1.-x2*
&(3*R+z)/R2/Rz))
 t1(p)=sqrt(1.0-p**2)
 t2(p)=sqrt(1.0-p**2)-sa*sqrt(1.0-(p/sa)**2)
 t22(p)=sqrt(1.0-P**2)-sa2*sqrt(1.0-(p/sa2)**2)
 t23(p)=sqrt(1.0-p**2)-sa3*sqrt(1.0-(p/sa3)**2)
 q(p)=sqrt(1.0-p**2)
 f=0.30
 f1=0.295
 f2=0.26
 f3=0.22
 sa=(1.0-(f1/f))**0.333
 sa2=(1.0-(f2/f))**0.333
 sa3=(1.0-(f3/f))**0.333

 xx=1.9
 do 6000 i=1,20
 z=0.02
 yy=0.0

 sgxx=0.0
 sgyy=0.0
 sgzz=0.0
 sgxy=0.0
 sgyz=0.0
 sgxz=0.0

 sgxx2=0.0
 sgyy2=0.0
 sgzz2=0.0
 sgxy2=0.0
 sgyz2=0.0
 sgxz2=0.0

 sgxx3=0.0
 sgyy3=0.0
 sgzz3=0.0
 sgxy3=0.0
 sgyz3=0.0
 sgxz3=0.0
```

```
      snxx=0.0
      snyy=0.0
      snzz=0.0
      snxy=0.0
      snyz=0.0
      snxz=0.0

      x1=1.0
      do 100 j=1,41

      ye=sqrt(1.0-x1**2)
      ye1=sqrt(sa**2-x1**2)
      ye2=sqrt(sa2**2-x1**2)
      ye3=sqrt(sa3**2-x1**2)

      c1=abs(x1)
      if(c1.lt.sa) go to 1
      ye1=0.0
    1 continue
      if(c1.lt.sa2) go to 3
      ye2=0.0
    3 continue
      if(c1.lt.sa3) go to 4
      ye3=0.0
    4 continue

      i=int(ye/0.05+0.5)
      y1=i*0.05
      i=2*i+1
      do 101 k=1,i

      p=sqrt(x1**2+y1**2)
      x=xx-x1
      y=yy-y1
      r=sqrt(x**2+y**2)
      R=sqrt(x**2+y**2+z**2)
      R3=R**3
      R5=R**5
      Rz=R+z
      x2=x**2
      y2=y**2
      z2=z**2
      z3=z**3
      R2=R**2
```

```
      A=t1(p)
      b=abs(y1)-ye1
      if(b.gt.0.0) go to 2
      A=t2(p)
    2 continue
      A2=t1(p)
      b2=abs(y1)-ye2
      if(b2.gt.0.0) go to 5
      A2=t22(p)
    5 continue
      A3=t1(p)
      b3=abs(y1)-ye3
      if(b3.gt.0.0) go to 6
      A3=t23(p)
    6 continue

      d=0.05**2
      c=q(p)

      sihxx=hxx(x2,z,R,R2,R3,R5,Rz)*c*d
      sihyy=hyy(y2,z,R,R2,R3,R5,Rz)*c*d
      sihzz=hzz(z3,R5)*c*d
      sihxy=hxy(x,y,z,R,R3,R5,Rz)*c*d
      sihyz=hyz(y,z2,R5)*c*d
      sihxz=hxz(x,z2,R5)*c*d


      G11=gxx(x,x2,z,R,R3,R5,Rz)
      G22=gyy(x,y2,z,R,R2,R3,R5,Rz)
      G33=gzz(x,z2,R5)
      G12=gxy(y,x2,z,R,R2,R5,Rz)
      G13=gxz(x2,z,R5)
      G23=gyz(x,y,z,R5)

      sigxx=G11*f*A*d
      sigyy=G22*f*A*d
      sigzz=G33*f*A*d
      sigxy=G12*f*A*d
      sigyz=G23*f*A*d
      sigxz=G13*f*A*d

      sigxx2=G11*f*A2*d
      sigyy2=G22*f*A2*d
      sigzz2=G33*f*A2*d
      sigxy2=G12*f*A2*d
      sigyz2=G23*f*A2*d
      sigxz2=G13*f*A2*d

      sigxx3=G11*f*A3*d
      sigyy3=G22*f*A3*d
      sigzz3=G33*f*A3*d
      sigxy3=G12*f*A3*d
      sigyz3=G23*f*A3*d
      sigxz3=G13*f*A3*d
```

```
      snxx=s1nxx+shxx
      snyy=s1nyy+shyy
      snzz=s1nzz+shzz
      snxy=s1nxy+shxy
      snyz=s1nyz+shyz
      snxz=s1nxz+shxz

      sgxx=s1gxx+sgxx
      sgyy=s1gyy+sgyy
      sgzz=s1gzz+sgzz
      sgxy=s1gxy+sgxy
      sgyz=s1gyz+sgyz
      sgxz=s1gxz+sgxz

      sgxx2=s1gxx2+sgxx2
      sgyy2=s1gyy2+sgyy2
      sgzz2=s1gzz2+sgzz2
      sgxy2=s1gxy2+sgxy2
      sgyz2=s1gyz2+sgyz2
      sgxz2=s1gxz2+sgxz2

      sgxx3=s1gxx3+sgxx3
      sgyy3=s1gyy3+sgyy3
      sgzz3=s1gzz3+sgzz3
      sgxy3=s1gxy3+sgxy3
      sgyz3=s1gyz3+sgyz3
      sgxz3=s1gxz3+sgxz3

  101 yl=y1-0.05
  100 xl=x1-0.05

      sxx=sgxx+snxx
      syy=sgyy+shyy
      szz=sgzz+snzz
      sxy=sgxy+shxy
      syz=sgyz+snyz
      sxz=sgxz+shxz

      sxx2=sgxx2+shxx
      syy2=sgyy2+shyy
      szz2=sgzz2+shzz
      sxy2=sgxy2+shxy
      syz2=sgyz2+snyz
      sxz2=sgxz2+shxz

      sxx3=sgxx3+shxx
      syy3=sgyy3+shyy
      szz3=sgzz3+shzz
      sxy3=sgxy3+shxy
      syz3=sgyz3+snyz
      sxz3=sgxz3+shxz
```

```
      sigma1=(sxx+szz)/2.0+sqrt(((sxx-szz)/2.0)**2+sxz**2)
      sigma2=(sxx2+szz2)/2.0+sqrt(((sxx2-szz2)/2.0)**2+sxz2**2)
      sigma3=(sxx3+szz3)/2.0+sqrt(((sxx3-szz3)/2.0)**2+sxz3**2)
      sigma0=(shxx+shzz)/2.0+sqrt(((shxx-shzz)/2.0)**2+shxz**2)

      sigm03=(shxx+shzz)/2.0-sqrt(((shxx-shzz)/2.0)**2+shxz**2)
      sigm13 =(sxx+szz)/2.0-sqrt(((sxx-szz)/2.0)**2+sxz**2)
      sigm23 =(sxx2+szz2)/2.0-sqrt(((sxx2-szz2)/2.0)**2+sxz2**2)
      sigm33 =(sxx3+szz3)/2.0-sqrt(((sxx3-szz3)/2.0)**2+sxz3**2)

      sigm02=shxx+shyy+shzz-sigma0-sigm03
      sigm12=sxx+syy+szz-sigma1-sigm13
      sigm22=sxx2+syy2+szz2-sigma2-sigm23
      sigm32=sxx3+syy3+szz3-sigma3-sigm33

      write(6,60) xx,yy,z,sigma0,sigma1,sigma2,sigma3
   60 format(/1X,3(F5.2,2X),4(E11.4,3X))

      write(6,71) sigm02,sigm12,sigm22,sigm32,sigm03,sigm13,sigm23,sigm3
     &3
   71 format(2(/22X,4(E11.4,3X)))

      e0=sqrt((shxx-shyy)**2+(shyy-shzz)**2+(shxx-shzz)**2+6.*(shxy**2+s
     &hxz**2+shyz**2))/1.414
      e1=sqrt((sxx-syy)**2+(syy-szz)**2+(szz-sxx)**2+6.*(sxy**2+syz**2+s
     &xz**2))/1.414
      e2=sqrt((sxx2-syy2)**2+(syy2-szz2)**2+(sxx2-szz2)**2+6.*(sxy2**2+s
     &xz2**2+syz2**2))/1.414
      e3=sqrt((sxx3-syy3)**2+(syy3-szz3)**2+(sxx3-szz3)**2+6.*(sxy3**2+s
     &xz3**2+syz3**2))/1.414

      write(6,65) e0,e1,e2,e3
   65 format(/15x,4(E11.4,5X))


 9000 xx=xx-0.2
      stop
      end
```

REFERENCES

[1] Auerbach, F. *Ann. Phys. Chem.* **43** (1891), 61.

[2] Griffith, A. A. *Phil. Trans.* A **221** ,(1920) 163.

[3] Fisher, J. C., and Holloman, J. H., *Metals Tech.* **14** (1947) 2218.

[4] Gibbs, P., and Culter, I.B., *J. Amer. Ceram. Soc.* **34** (1951) 200.

[5] Roesler, F.C., *Proc. Phys. Soc.* B **69** (1956a) 55.

[6] Frank, F.C., and Lawn, B.R., *Proc. R. Soc. Lond.* , A **299** (1967) 291.

[7] Hamilton, G.M., and Goodman, L.E., *Trans. Am. Soc. Metals,* **33** , (1966), 371.

[8] Lawn, B.R., *Proc. R. Soc. Lond.,* A **299** (1967) 307.

[9] Gilroy, D.R., and Hirst, W., *J. Phys. D: Appl. Phys.,* **2** (1969), 1784.

[10] Chiang, S.S., and Evans, A.G., *J. Amer. Ceram. Soc.* **66** (1983) 4.

[11] Boussinesq, J., see Timoshenko, S. and Goodier, J.N. *Theory of Elasticity* (McGraw Hill) 1950 pp. 39-40.

[12] Mindlin, R.D., *Physics,* 7 (1936) 85.

[13] Hertz, H., *Hertz's Miscellaneous Papers* , Chapter 5 and 6, (London Macmillan).

[14] Mindlin, R.D., *J. Appl. Mech. Trans.* **ASME 71** (1949) 259.

[15] Morton, W.B. and Close, I.J., *Phil. Mag.* **43** (1922) 320.

[16] Evans, A.G., *J. Amer. Ceram. Soc.* **57** (1974) 410.

[17] Lawn, B.R., and Komatsu, H., *Phil. Mag.* **68** (1966) 689.

[18] Lawn, B.R., and Wilshaw, T.R., *Fracture of Brittle Solids* (Cambridge University Press).

[19] Marshall, D.B. and Lawn. B.R., *J. Mat. Sci.* **14** (1979) 2001.

[20] Chiang, S.S., Marshall, D.B., and Evans, A.G., *J. Appl. Phys.* **53** (1982) 298.

[21] Hertzberg, R.W. *Deformation and Fracture Mechanics of Engineering Materials* 2nd ed. (1983), (John Wiely and Sons).

[22] Bates, R.C., and Clark, W.G.Jr., *Trans. Quart* **ASM 62** (1969) 380.

[23] Lawn, B.R., and Evans, A.G., *J. Amer. Ceram. Soc.* **63** (1980) 574; Marshall, D.B., and Lawn, B.R., and Evans, .A.G., *J. Amer. Ceram. Soc.* **65** (1982) 561.

Table I. Contact Characteristics

Normal load (N)	radius of contact area (μm)	maximum normal pressure, σ_o (GPa)
80	95.1	4.139
120	109.0	4.726
170	122.3	5.344
210	130.8	5.726
260	141.2	6.119

Table II. Maximum Calculated Shear Stresses*

maximum normal pressure σ_o (GPa)	loading ratio, P^s/P^n	calculated normalized maximum shear stresses, τ_{max}/σ_o	calculated maximum shear stresses, τ_{max} N
4.139	0.0	0.640	2.649
	0.22	0.655	2.711
	0.26	0.662	2.740
	0.295	0.675	2.794
4.726	0.0	0.640	3.025
	0.22	0.655	2.096
	0.26	0.662	3.129
	0.295	0.675	3.190
5.344	0.0	0.640	3.420
	0.22	0.655	3.500
	0.26	0.662	3.538
	0.295	0.675	3.607
5.726	0.0	0.640	3.665
	0.22	0.655	3.751
	0.26	0.662	3.791
	0.295	0.675	3.865
6.119	0.0	0.640	3.916
	0.22	0.655	4.008
	0.26	0.662	4.051
	0.295	0.675	4.130

*Yield strength of glass = 3.04 GPa [20]

FIGURE CAPTIONS

Fig.1. The model system is a ball in contact with a flat surface, subject to normal and tangential forces, where P^S and P^N are tangential and normal loads, respectively.

Fig.2. A schematic showing the partial slip condition and the resultant traction distribution at the interface, in cylindrical coordinstes, where τ_{zz} and τ_{zx} are normal and tangential surface tractions, respectively. a and a^* are the radii of partial slip and contact regions, respectively.

Fig.3. The trajectories of the maximum principal stress σ_1 in the x-z plane for normal loads, and the σ_3 stress trajectory starting from the edge of the circle of contact. The length is normalized by a and the stress by σ_o.

Fig.4. The σ_1 and σ_3 trajectories, starting from the point of the maximum tensile stress: loading ratio 0.22 and friction coefficient 0.3.

Fig.5. The σ_1 and σ_3 trajectories, starting from the point of maximum tensile stress: loading ratio 0.26 and friction coefficient 0.3.

Fig.6. The σ_1 and σ_3 trajectories, starting from the point of maximum tensile stress: loading ratio 0.295 and friction coefficient 0.3.

Fig.7. The effective shear stress distribution for normal loading.

Fig.8. The effective shear stress distribution for a loading ratio 0.22.

Fig.9. The effective shear stress distribution for a loading ratio 0.26.

Fig.10. The effective shear stress distribution for a loading ratio 0.295.

Fig.11. The experimental arrangement for coupled loading test.

Fig.12. The experimental arrangement for normal loading test.

Fig.13. The cyclic loading condition with a loading ratio of 0.26.

Fig.14. The loading condition for comparison of slow crack growth effect with cyclic effects.

Fig.15. Typical indentation crack morphologies on the bend test fracture surface. (a) single cycle (b) multiple cycles.

Fig.16. Weibull plot of probability against friction coefficient.

Fig.17. The failure strength from four-point bending tests as a function of the normal load during indentation test for various loading ratios (f=0.3).

Fig.18. The failure strength from four-point bending tests vs. the normal load for various cycles. (a) loading ratio=0.22 and friction coefficient=0.3. (b) loading ratio=0.26 and friction coefficient=0.3.

Fig.19. The failure strength from four-point bending tests vs. normal load for slow crack growth tests, compared with cyclic tests.

Fig.20. An SEM micrograph of first type fracture surface, relative to its schematic drawing.

Fig.21. Both sides of the cone crack, top view in (a) and bottom view in (b) for five cycles.

Fig.22. An SEM micrograph of the second type of fracture surface, relative to its schematic drawing.

Fig.23. A high magnification SEM picture of the fracture surface of a specimen failed after ten cycles empphasizing the cone crack tips.

Fig.24. The SEM picture of test specimen failed after five cycles with low magnification picture in (a) and high magnification picture in (b).

Fig.25. An SEM micrograph of the top view of the cone crack for a test specimen failed after 100 cycles with low magnification in (a) and high magnification in (b).

Fig.26. The SEM micrograph of the bottom view of the cone crack for a test specimen failed after 100 cycles with low magnification in (a) and high magnification in (b).

Fig.27. Interference micrograph of the indentation area.

Fig.28. The surface profile of the specimen surface along the contact area. Path of stylus cross the center of contact circle in the direction opposite to tangential load applied.

Fig.29. Striation spacing on cone crack surface vs. number of cycles.

Fig.30. Striation spacing on cone crack surface vs. stress intensity factor change.

Fig.31. The relative coordinates used for integration.

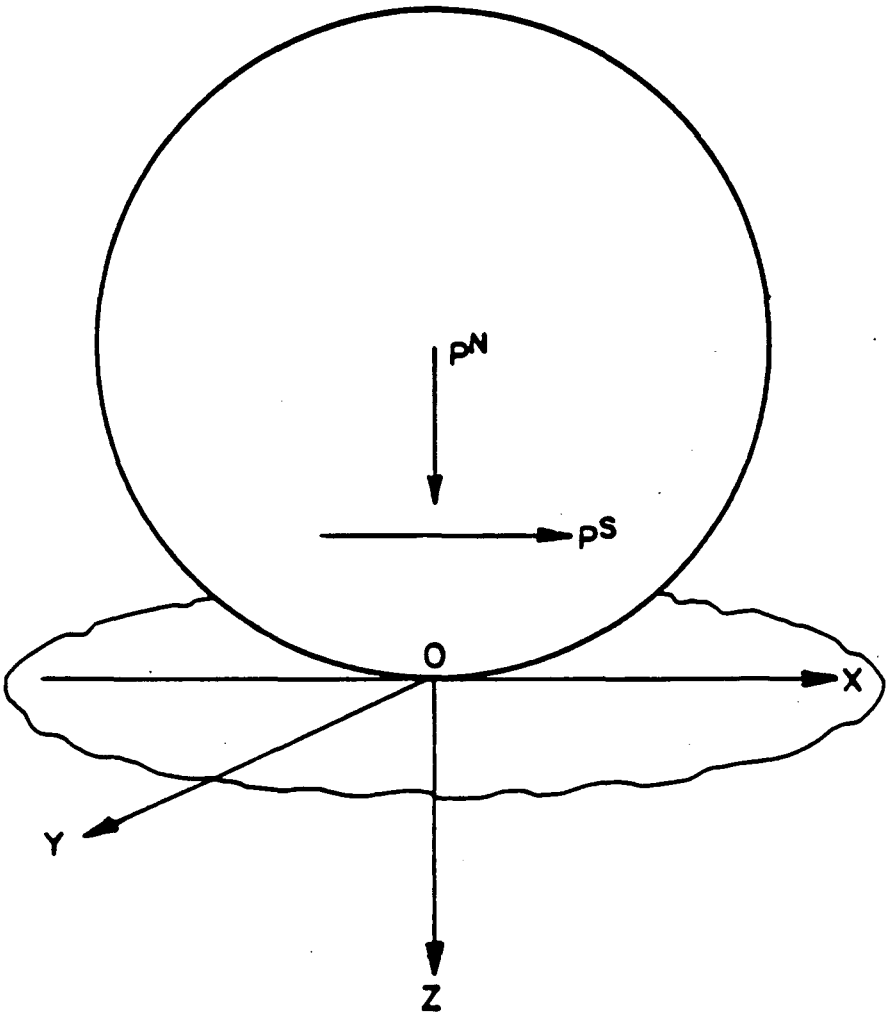

Figure 1

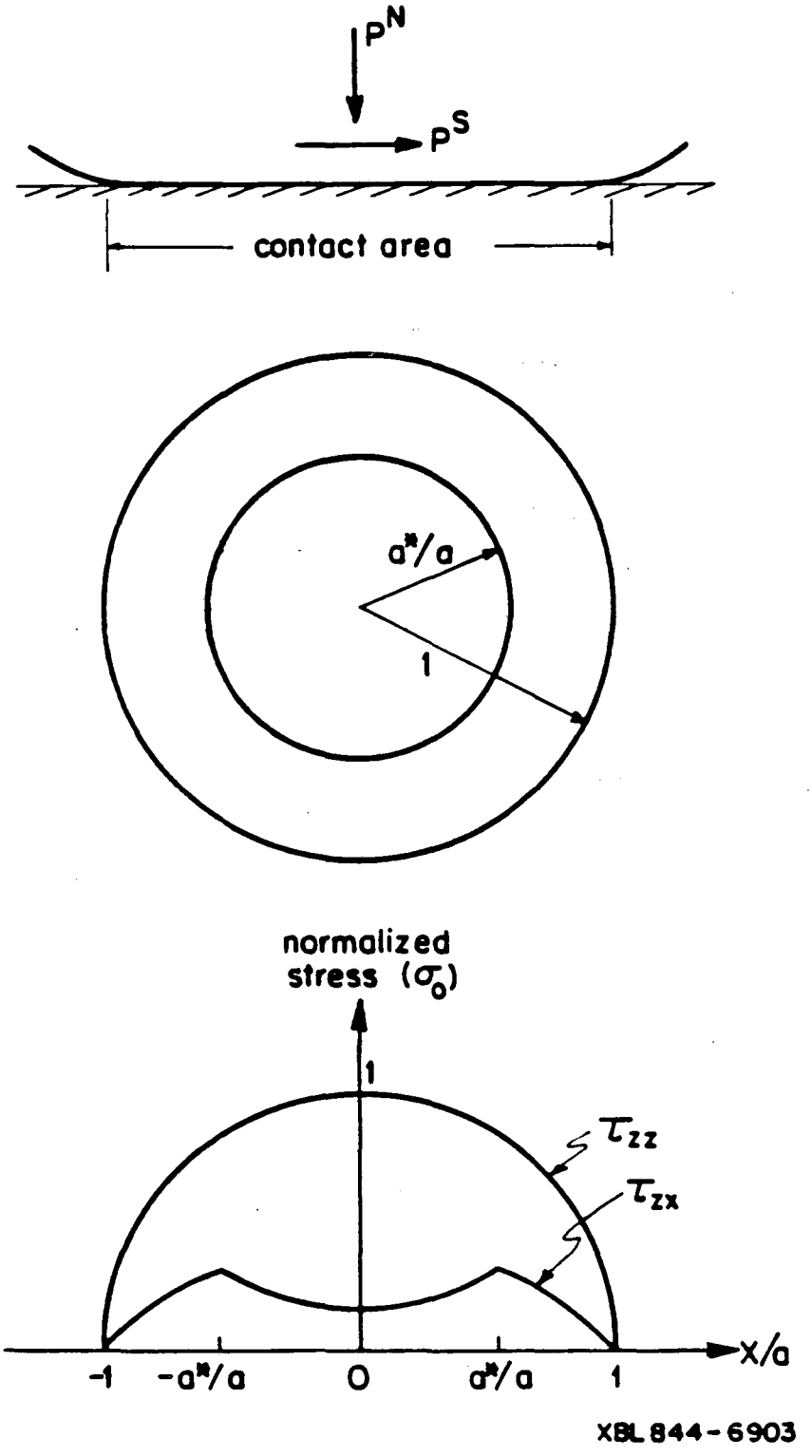
P^N
P^S
contact area
a*/a
1
normalized
stress (σ0)
1
τzz
τzx
-1
-a*/a
0
a*/a
1
X/a
XBL844-6903

Figure 2

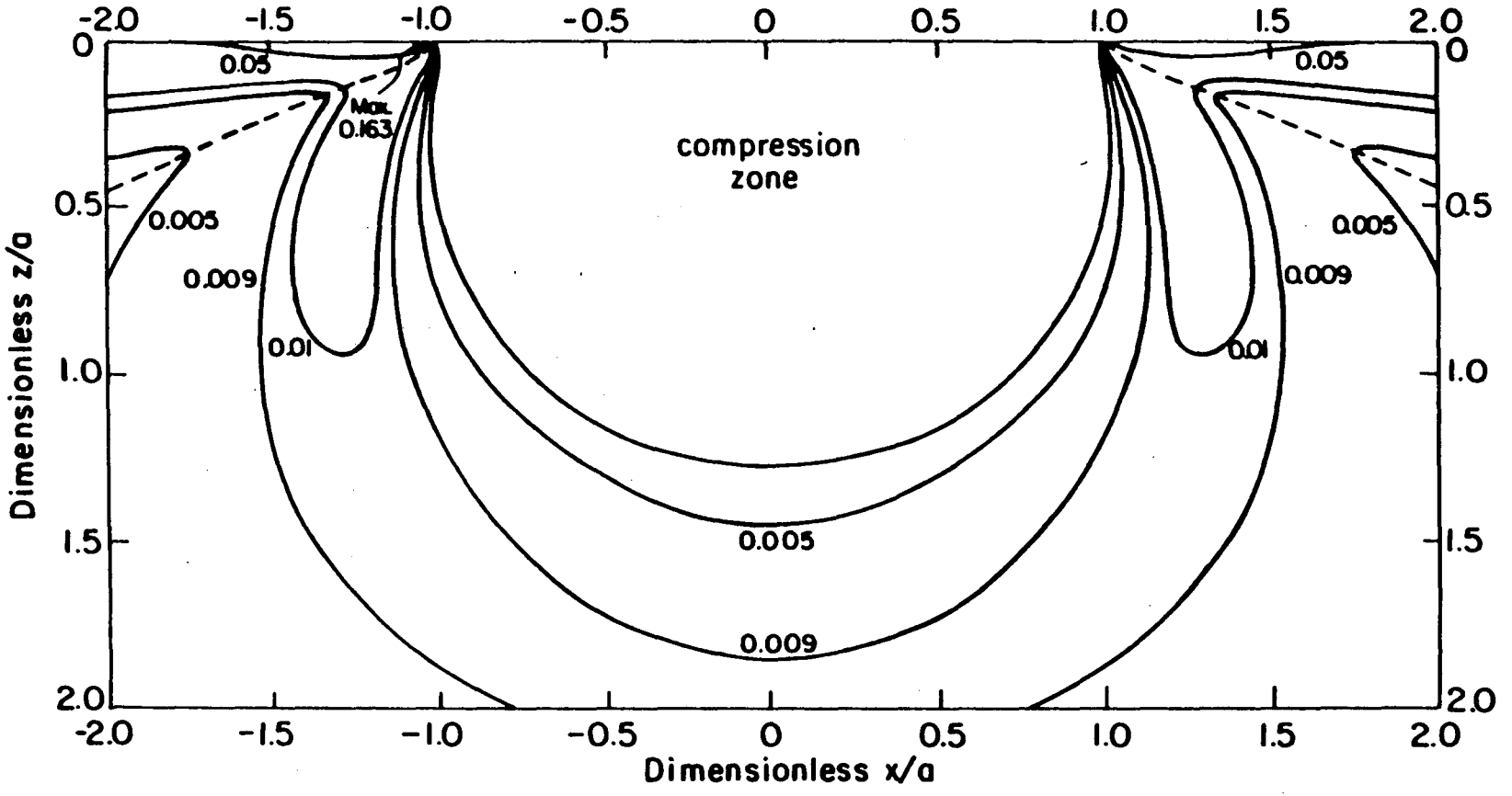
-2.0
-1.5
-1.0
-0.5
0
0.5
1.0
1.5
2.0
0.05
Max.
0.163
compression
zone
0.005
0.009
0.01
0.005
0.009
Dimensionless z/a
Dimensionless x/a
XBL844-6904

Figure 3

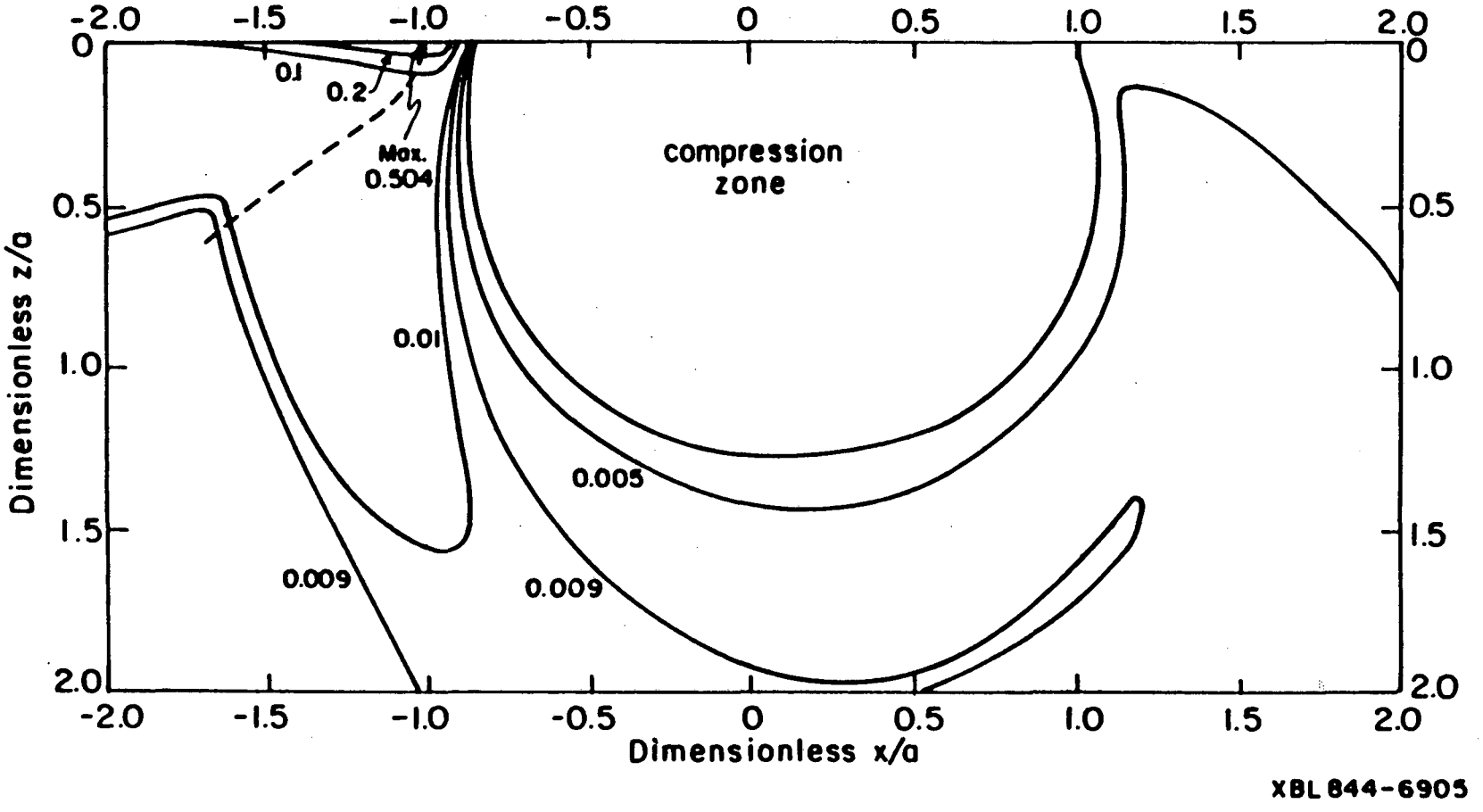
-2.0
-1.5
-1.0
-0.5
0
0.5
1.0
1.5
2.0
0.1
0.2
Max.
0.504
compression
zone
0.01
0.005
0.009
0.009
Dimensionless z/a
Dimensionless x/a
XBL 844-6905

Figure 4

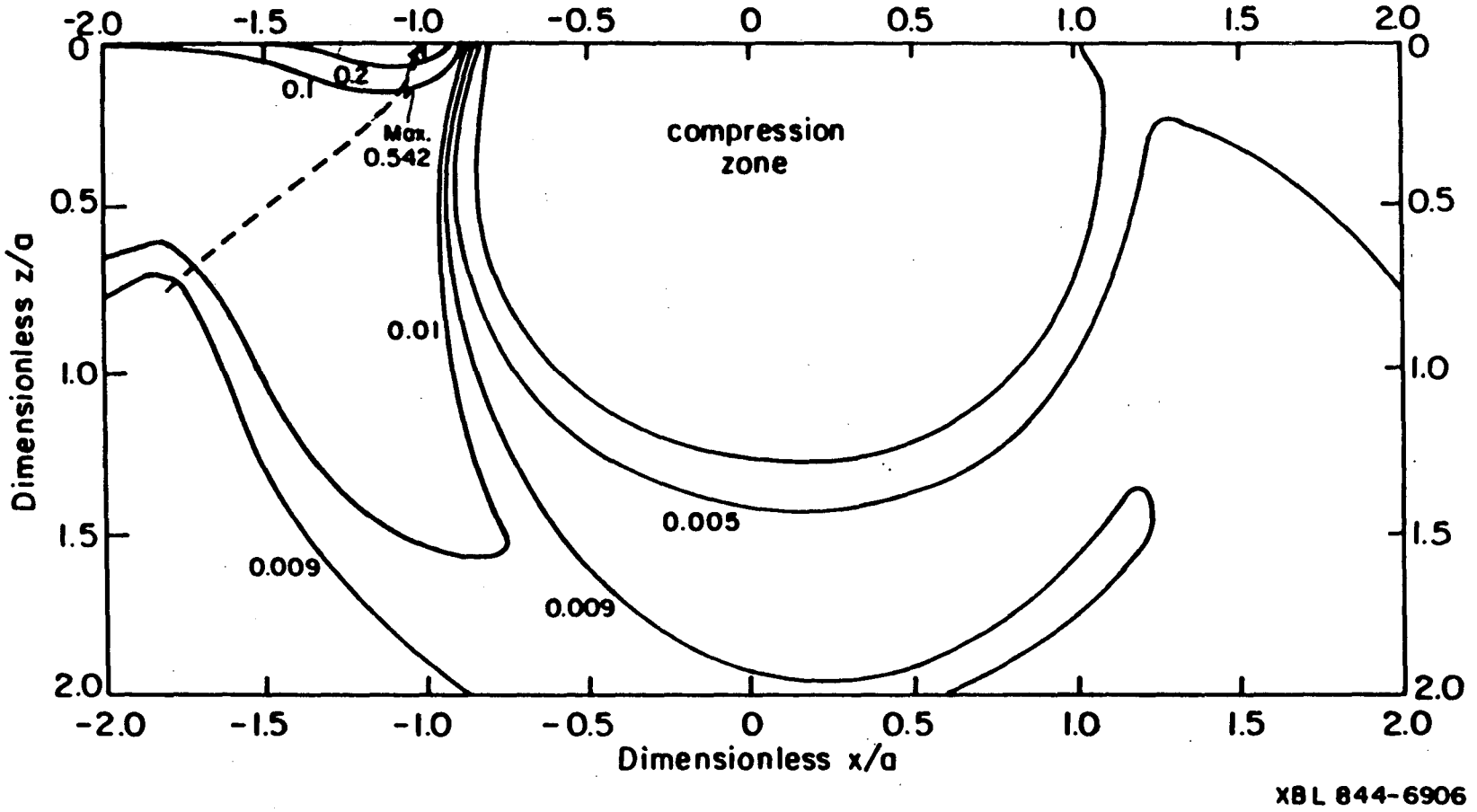
-2.0
-1.5
-1.0
-0.5
0
0.5
1.0
1.5
2.0
0
0.5
1.0
1.5
2.0
0.1
0.2
Max.
0.542
compression
zone
0.01
0.005
0.009
0.009
Dimensionless z/a
Dimensionless x/a
XBL 844-6906

Figure 5

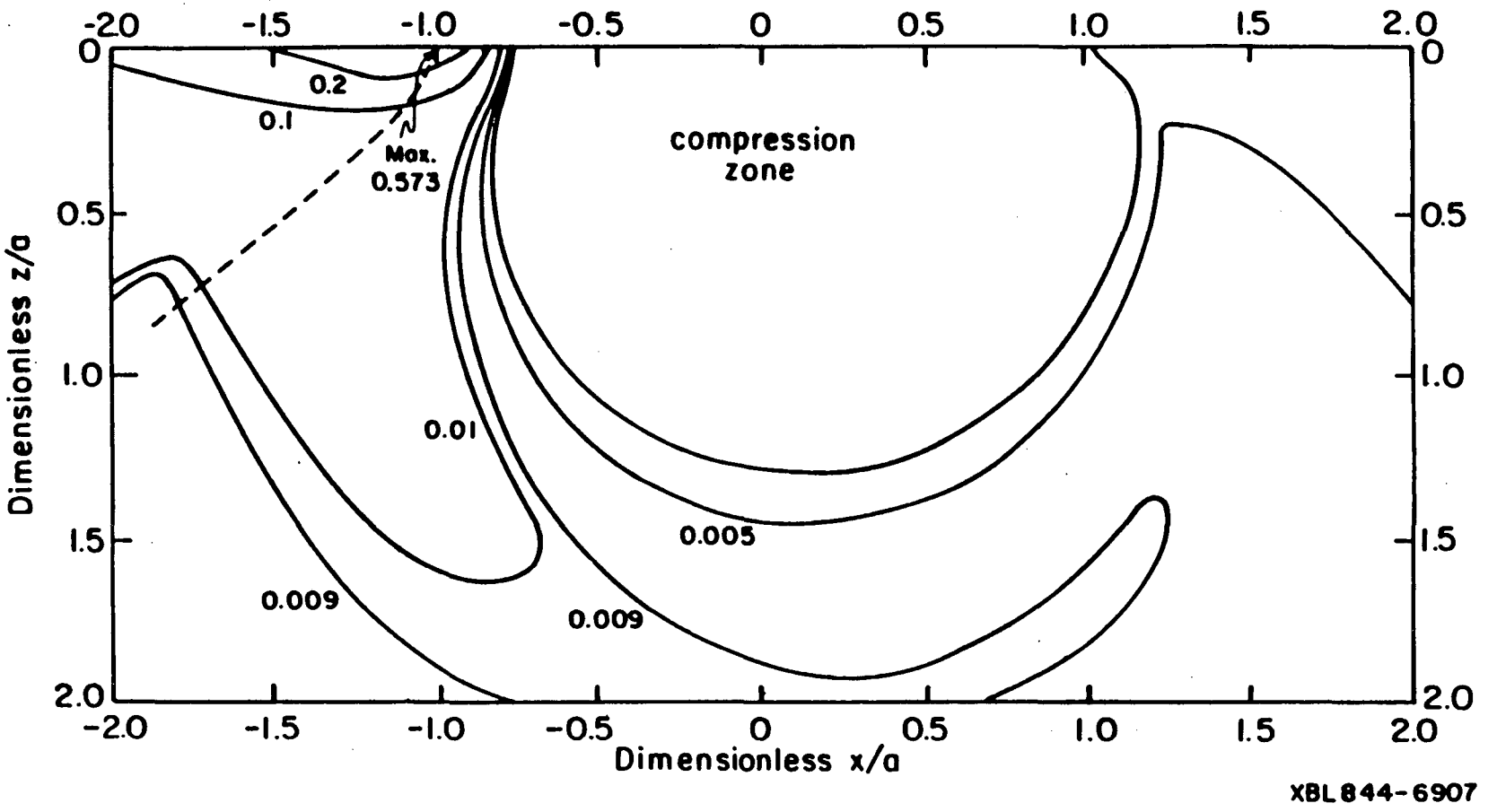
-2.0
-1.5
-1.0
-0.5
0
0.5
1.0
1.5
2.0
0.2
0.1
Max.
0.573
compression
zone
0.01
0.005
0.009
0.009
Dimensionless z/a
Dimensionless x/a
XBL844-6907

Figure 6

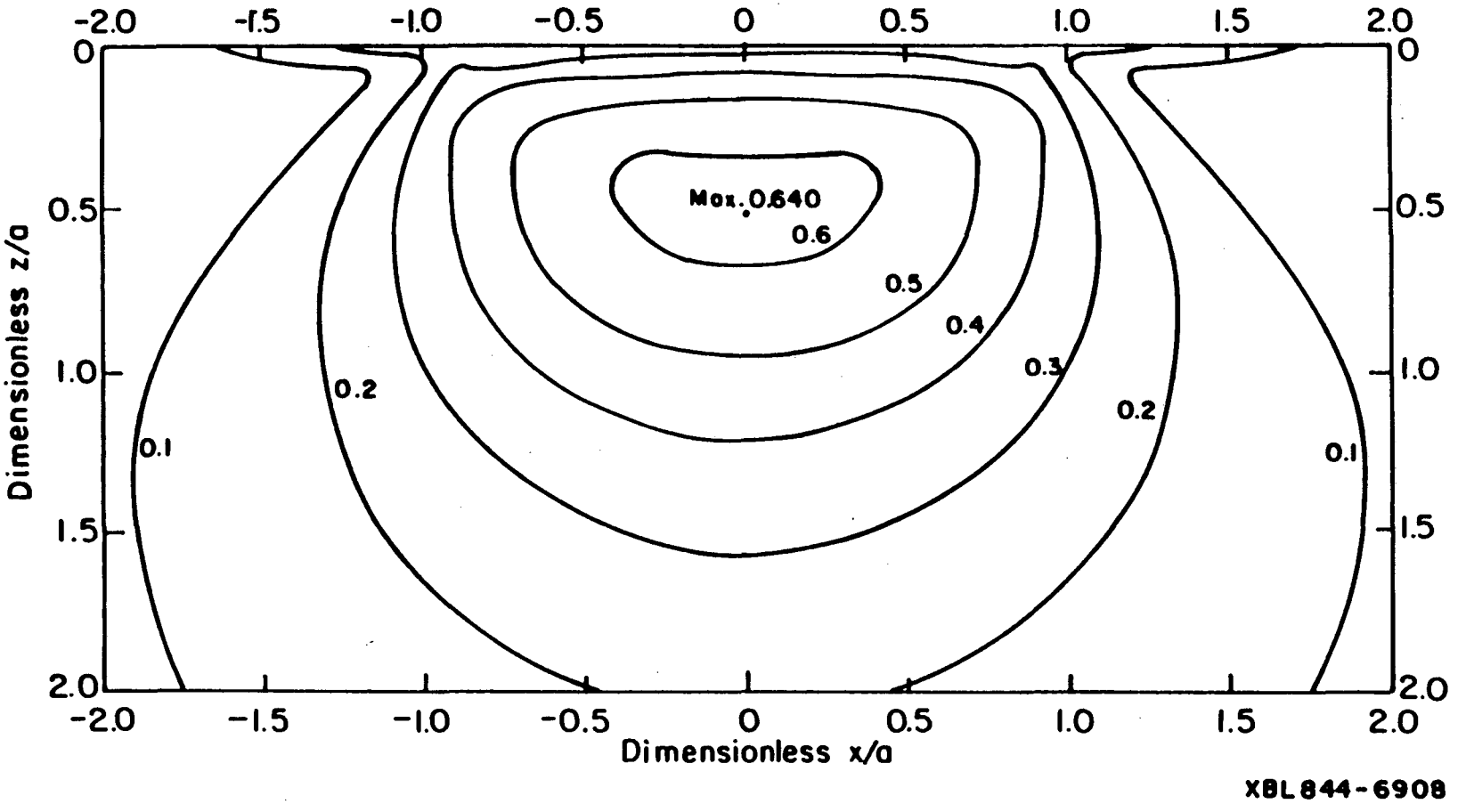
-2.0
-1.5
-1.0
-0.5
0
0.5
1.0
1.5
2.0
0
0.5
1.0
1.5
2.0
Max. 0.640
0.6
0.5
0.4
0.3
0.2
0.1
Dimensionless z/a
Dimensionless x/a
XBL844-6908

Figure 7

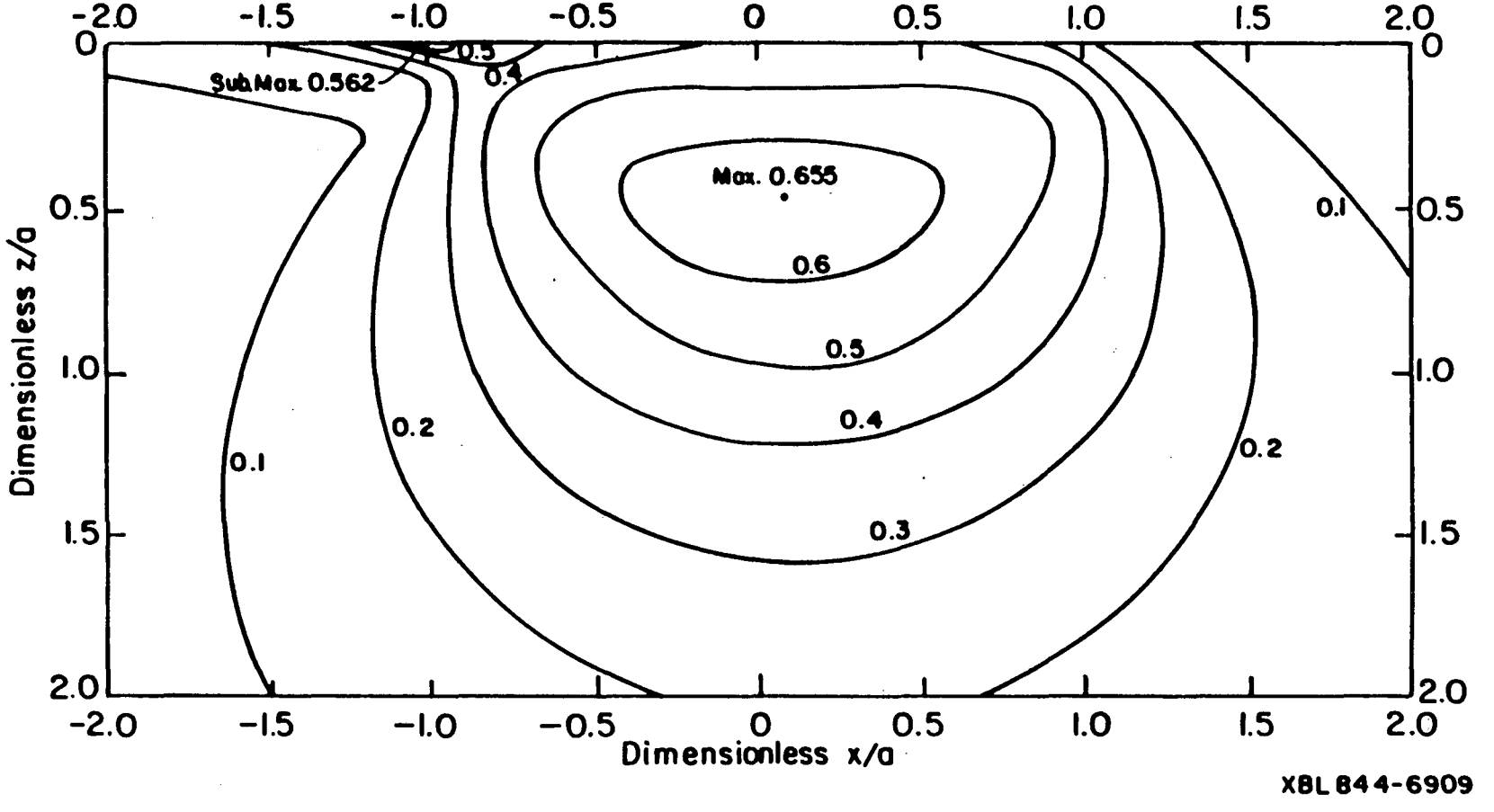
-2.0
-1.5
-1.0
-0.5
0
0.5
1.0
1.5
2.0
Sub Max. 0.562
0.5
0.4
Max. 0.655
0.6
0.5
0.4
0.3
0.2
0.1
0.2
0.1
Dimensionless z/a
Dimensionless x/a
XBL 844-6909

Figure 8

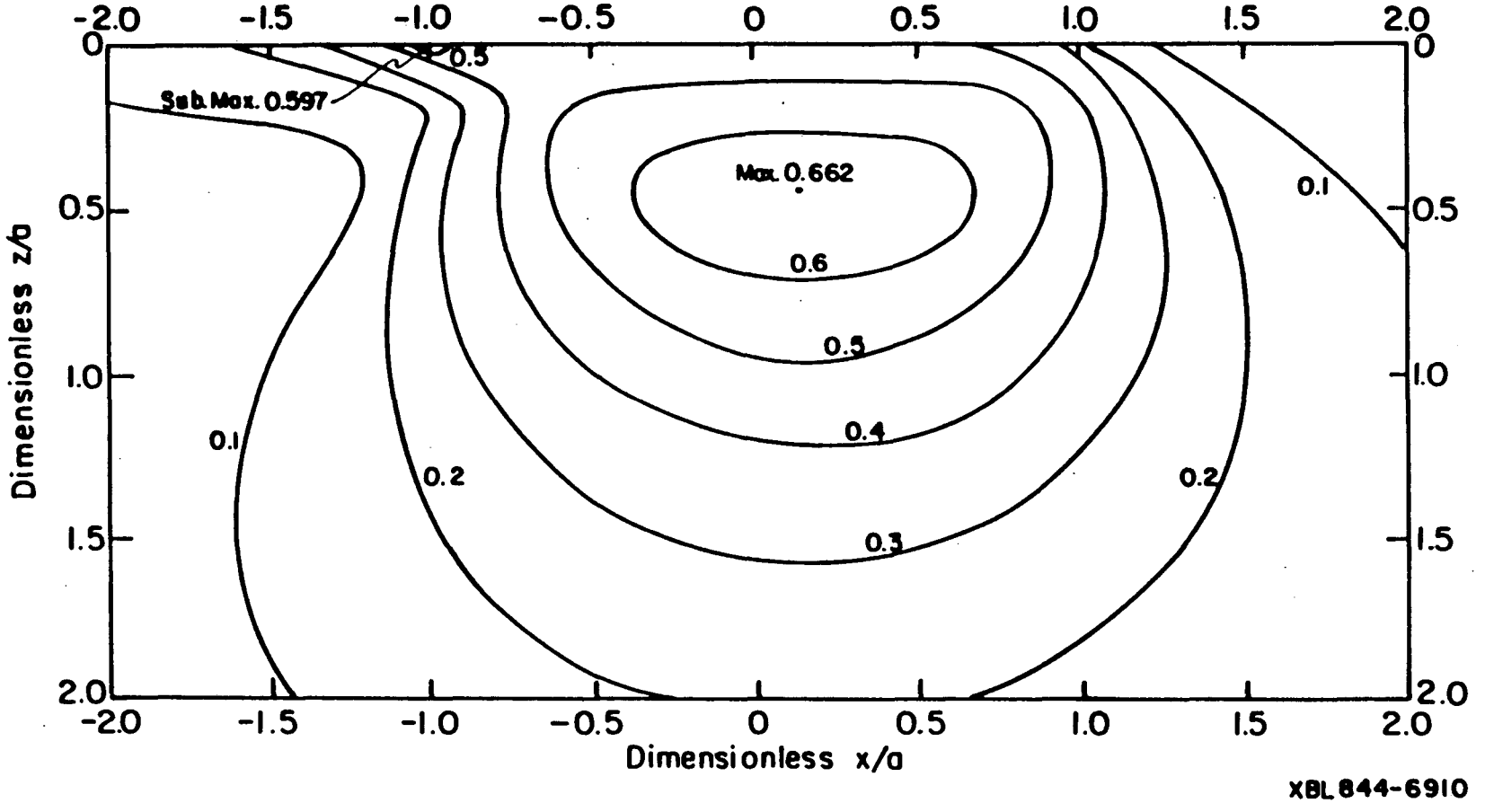
-2.0
-1.5
-1.0
-0.5
0
0.5
1.0
1.5
2.0
Sub. Max. 0.597
Max. 0.662
0.5
0.6
0.5
0.4
0.3
0.2
0.1
0.2
0.1
Dimensionless z/a
Dimensionless x/a
XBL 844-6910

Figure 9

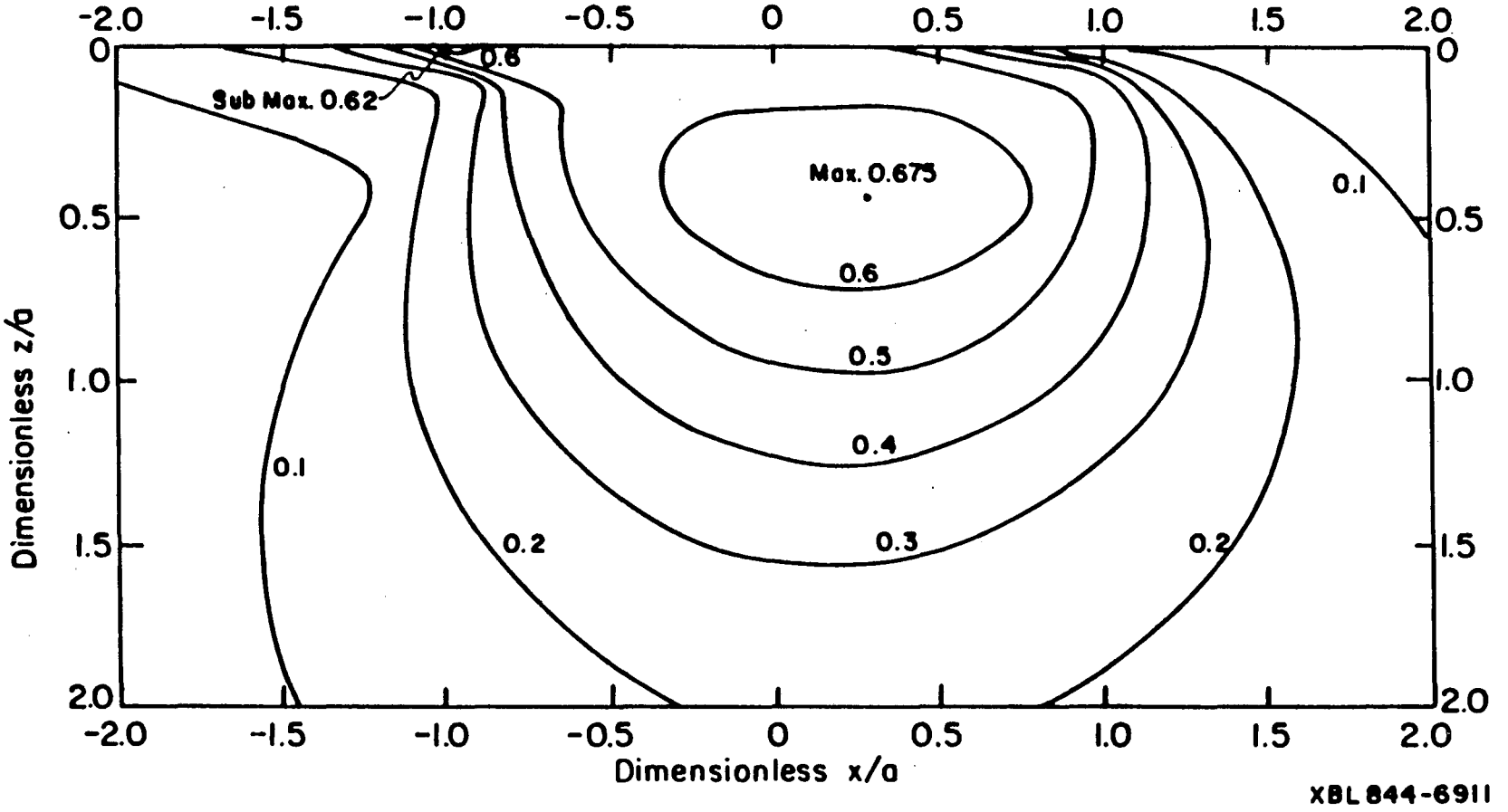
-2.0
-1.5
-1.0
-0.5
0
0.5
1.0
1.5
2.0
0
0.5
1.0
1.5
2.0
Sub Max. 0.62
0.6
Max. 0.675
0.6
0.5
0.4
0.3
0.2
0.1
0.2
0.1
Dimensionless z/a
Dimensionless x/a
XBL 844-6911

Figure 10

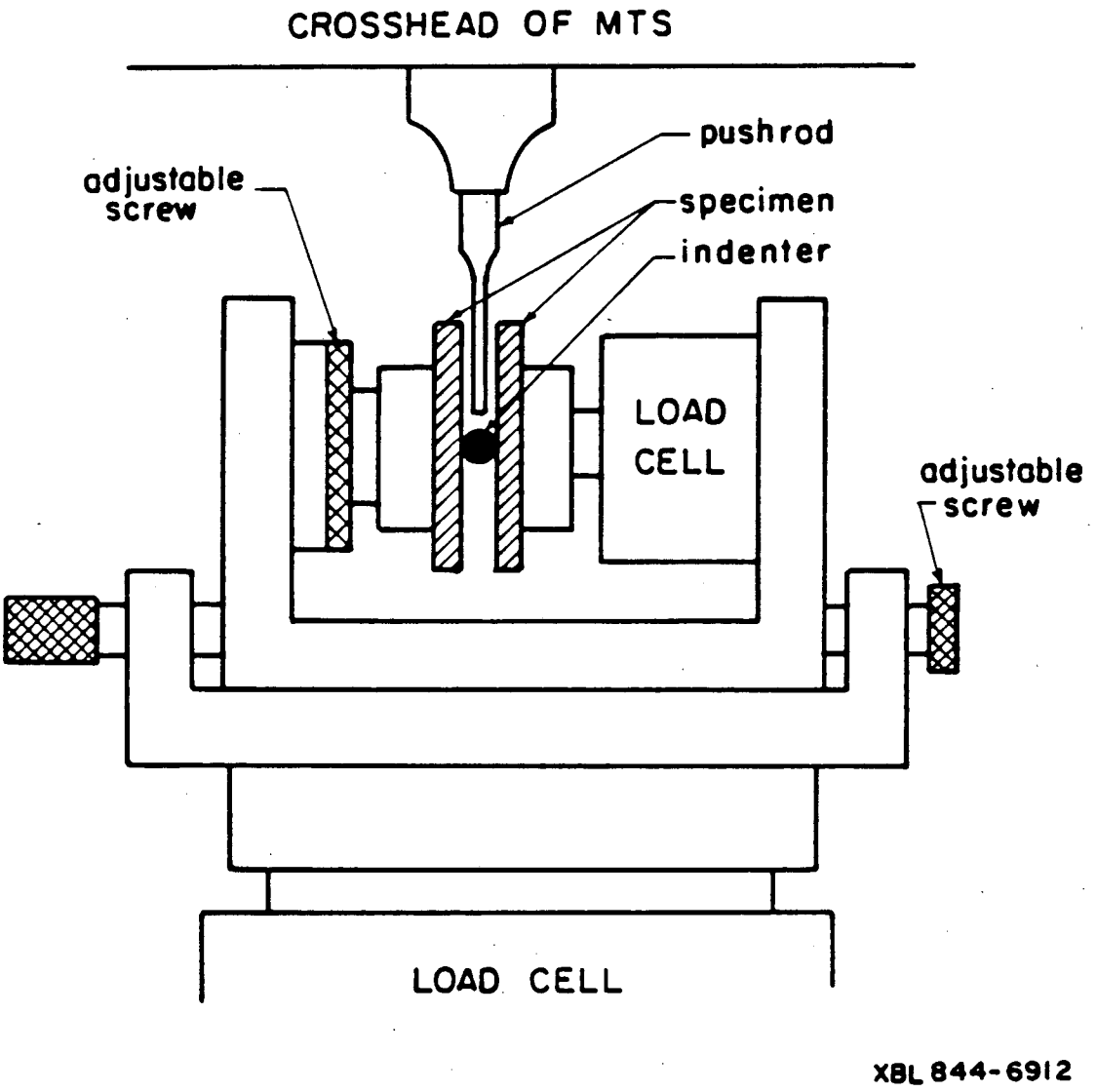
CROSSHEAD OF MTS
pushrod
adjustable screw
specimen
indenter
LOAD CELL
adjustable screw
LOAD CELL
XBL 844-6912

Figure 11

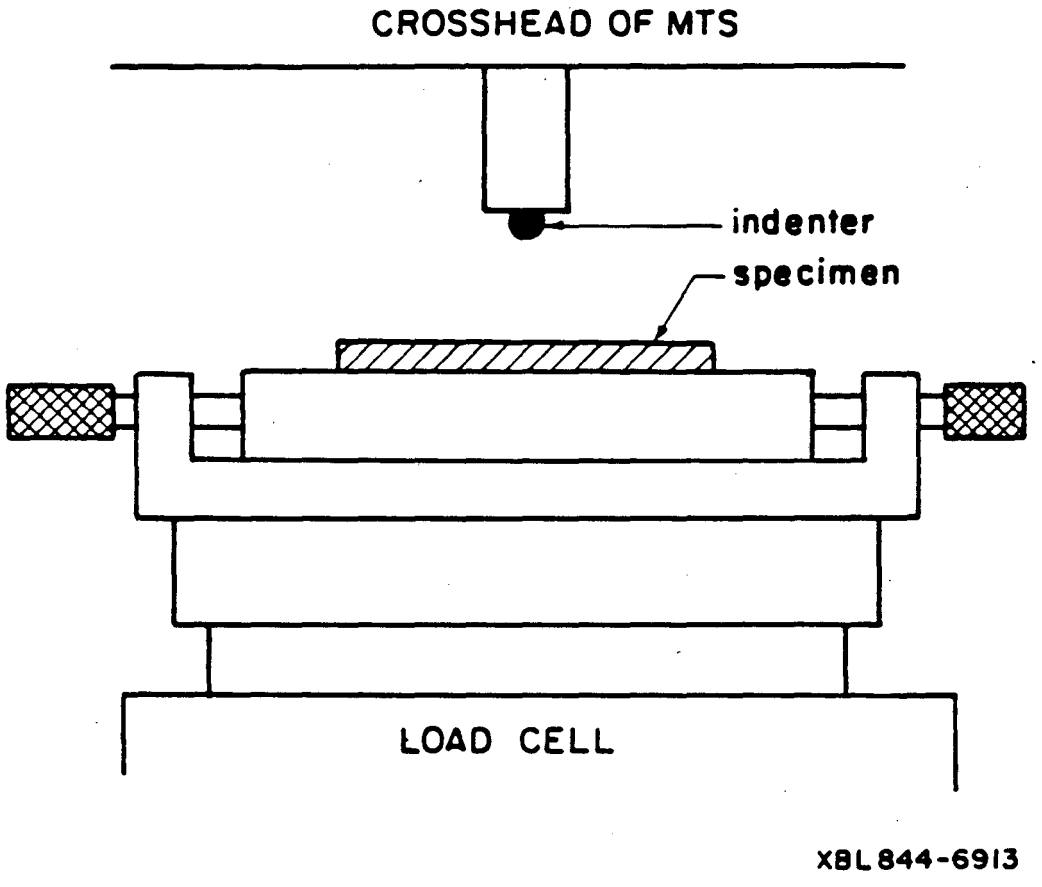

Figure 12

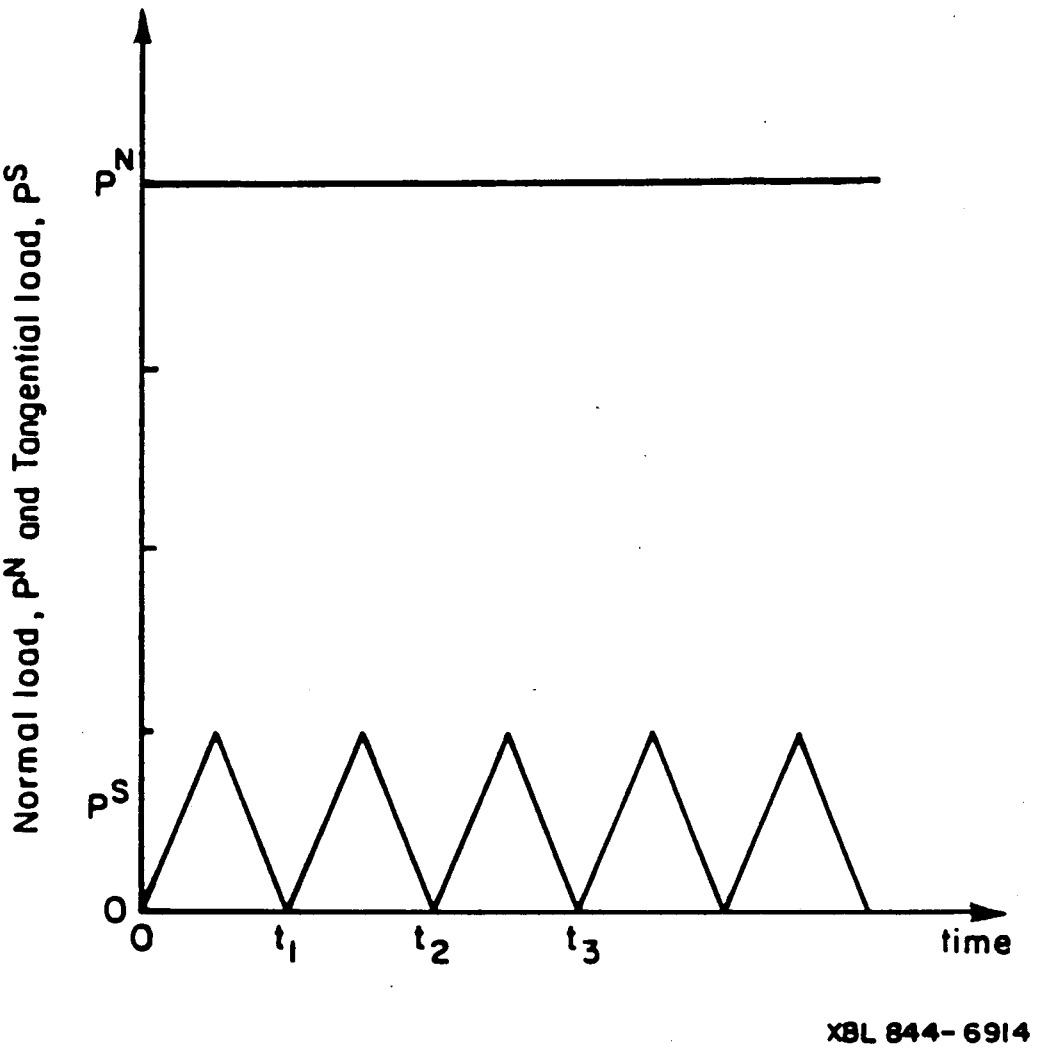
Normal load, P^N and Tangential load, P^S
P^N
P^S
0
0
t_1
t_2
t_3
time
XBL 844-6914

Figure 13

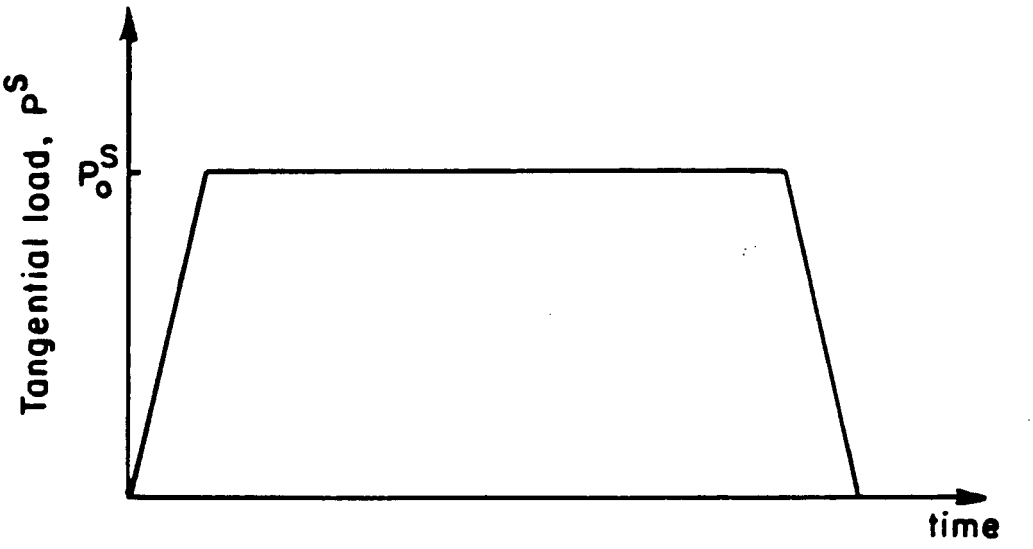

Slow crack growth test

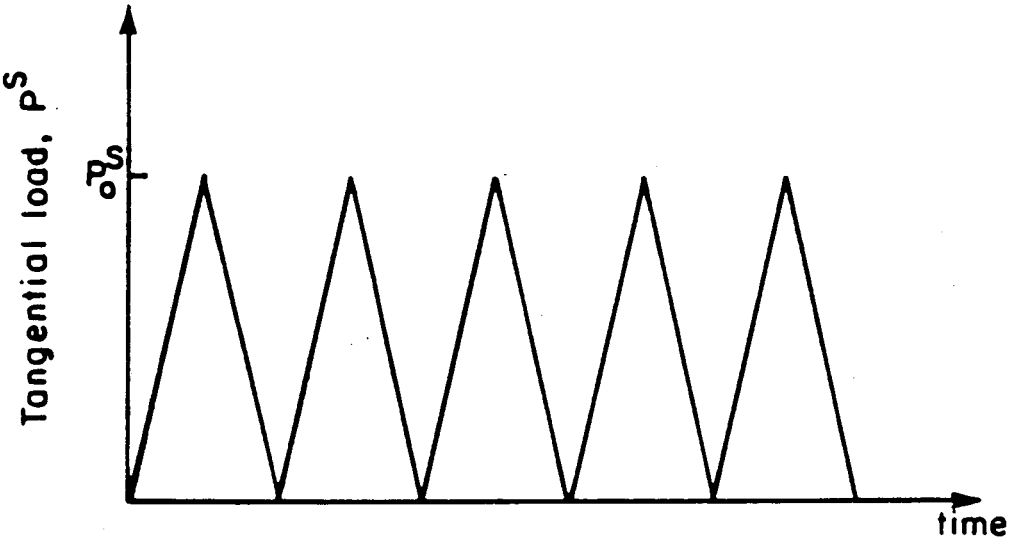

Cyclic loading test

XBL 844-6915

Figure 14

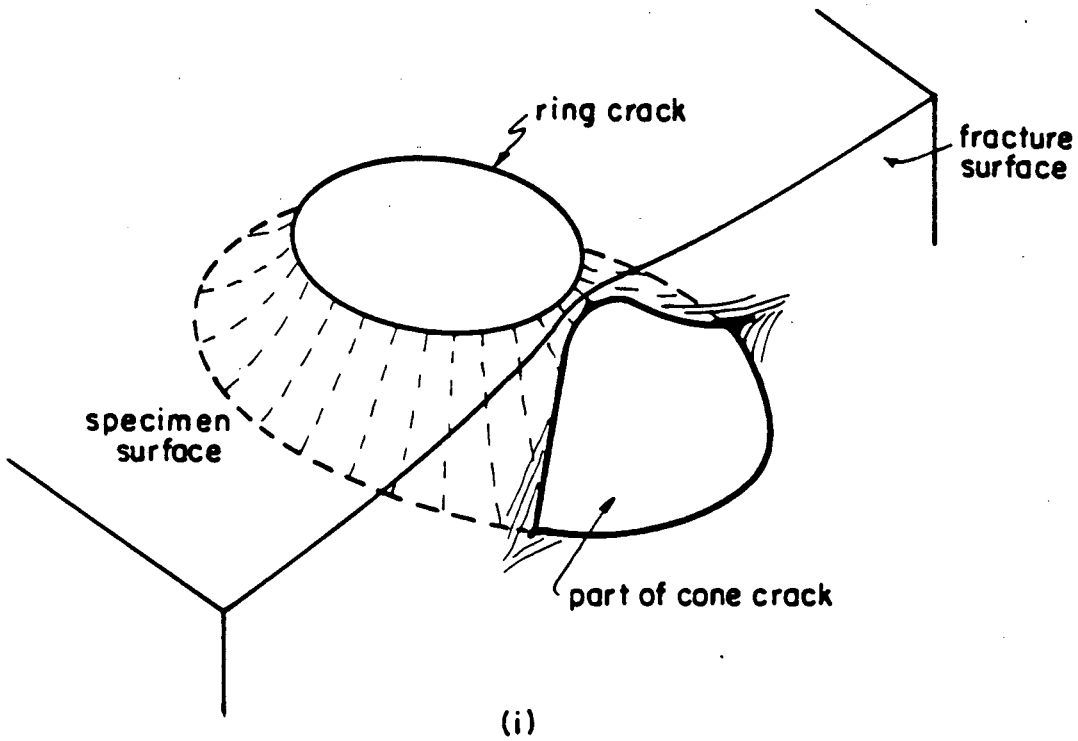

(i)

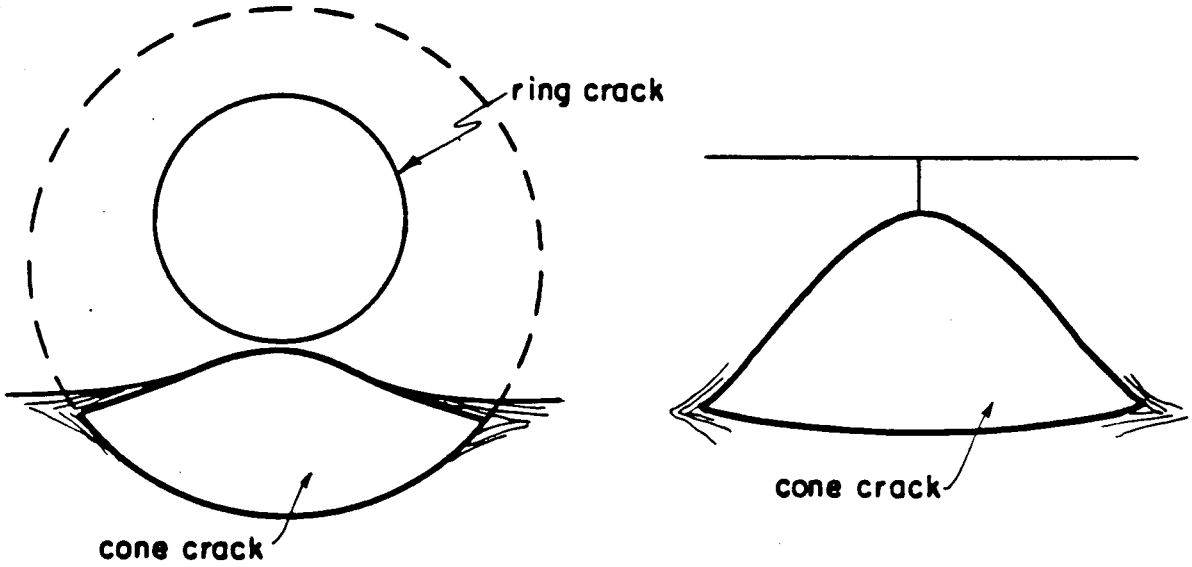

Top View

(ii)

Side View

(iii)

XBL 844-6916

Figure 15(a)

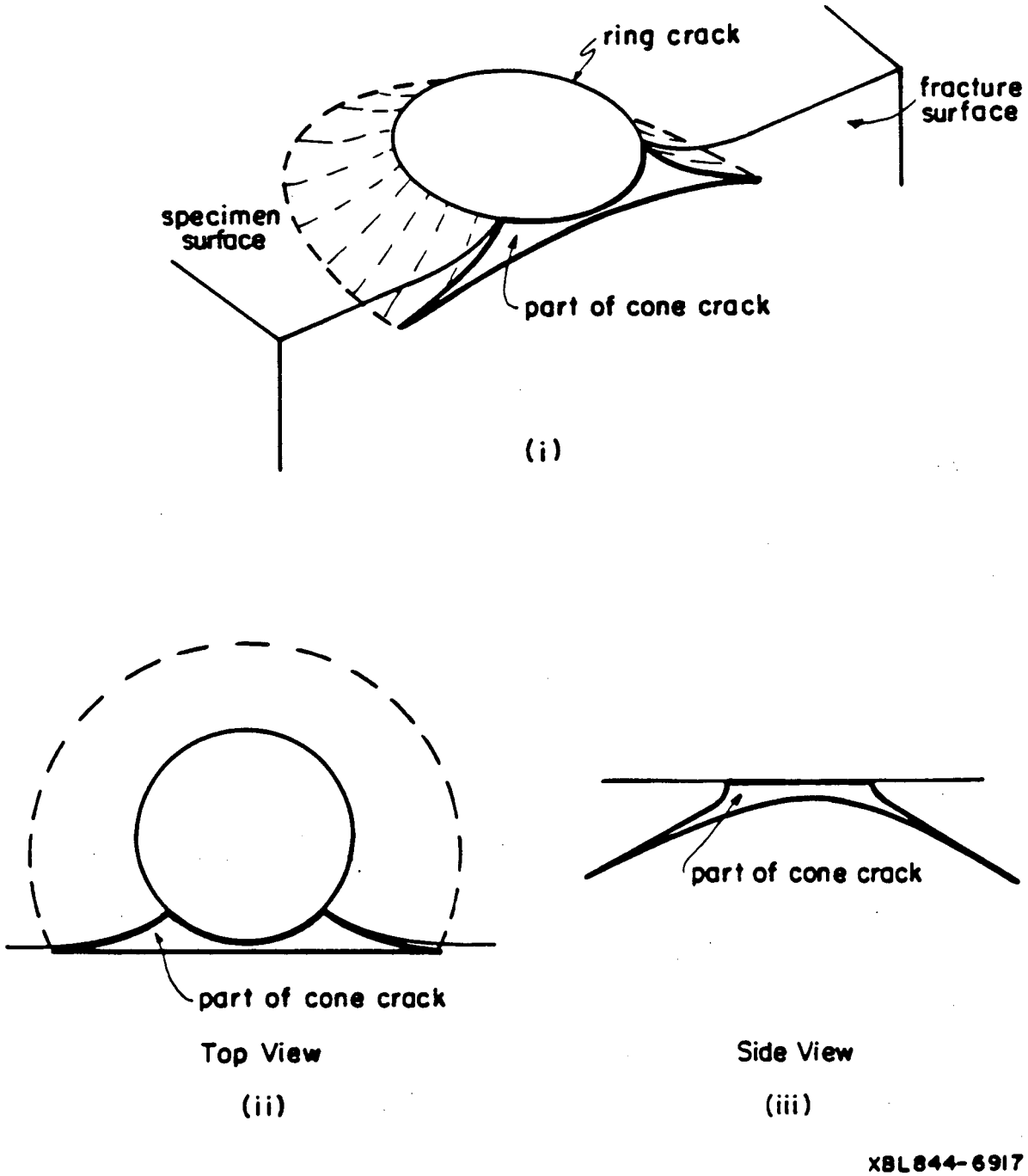
ring crack
fracture surface
specimen surface
part of cone crack
(i)
part of cone crack
Top View
(ii)
part of cone crack
Side View
(iii)
XBL844-6917

Figure 15(b)

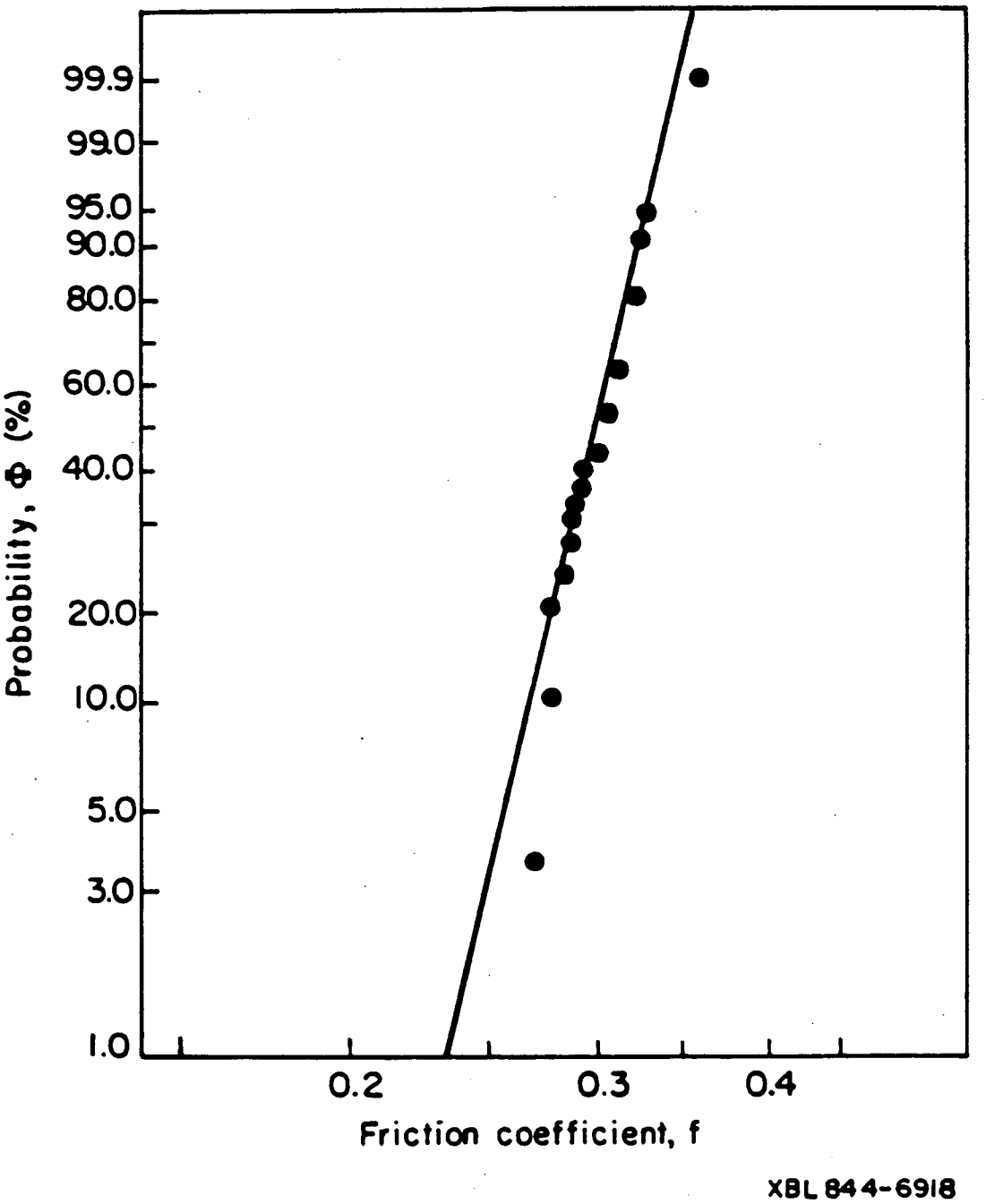
99.9
99.0
95.0
90.0
80.0
60.0
40.0
20.0
10.0
5.0
3.0
1.0
Probability, Φ (%)
0.2
0.3
0.4
Friction coefficient, f
XBL 844-6918

Figure 16

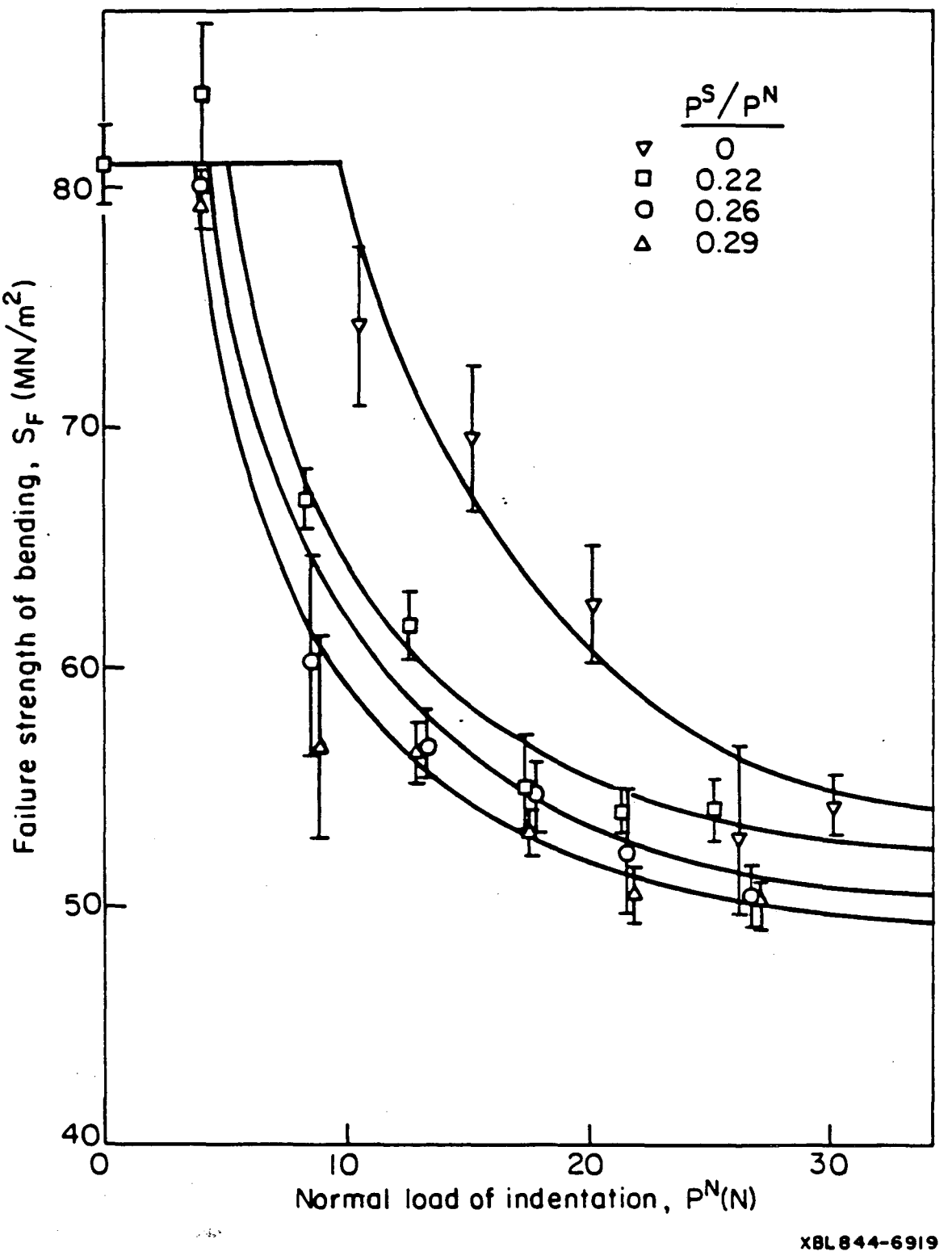
P^S/P^N
0
0.22
0.26
0.29
Failure strength of bending, S_F (MN/m^2)
80
70
60
50
40
0
10
20
30
Normal load of indentation, P^N(N)
XBL844-6919

Figure 17

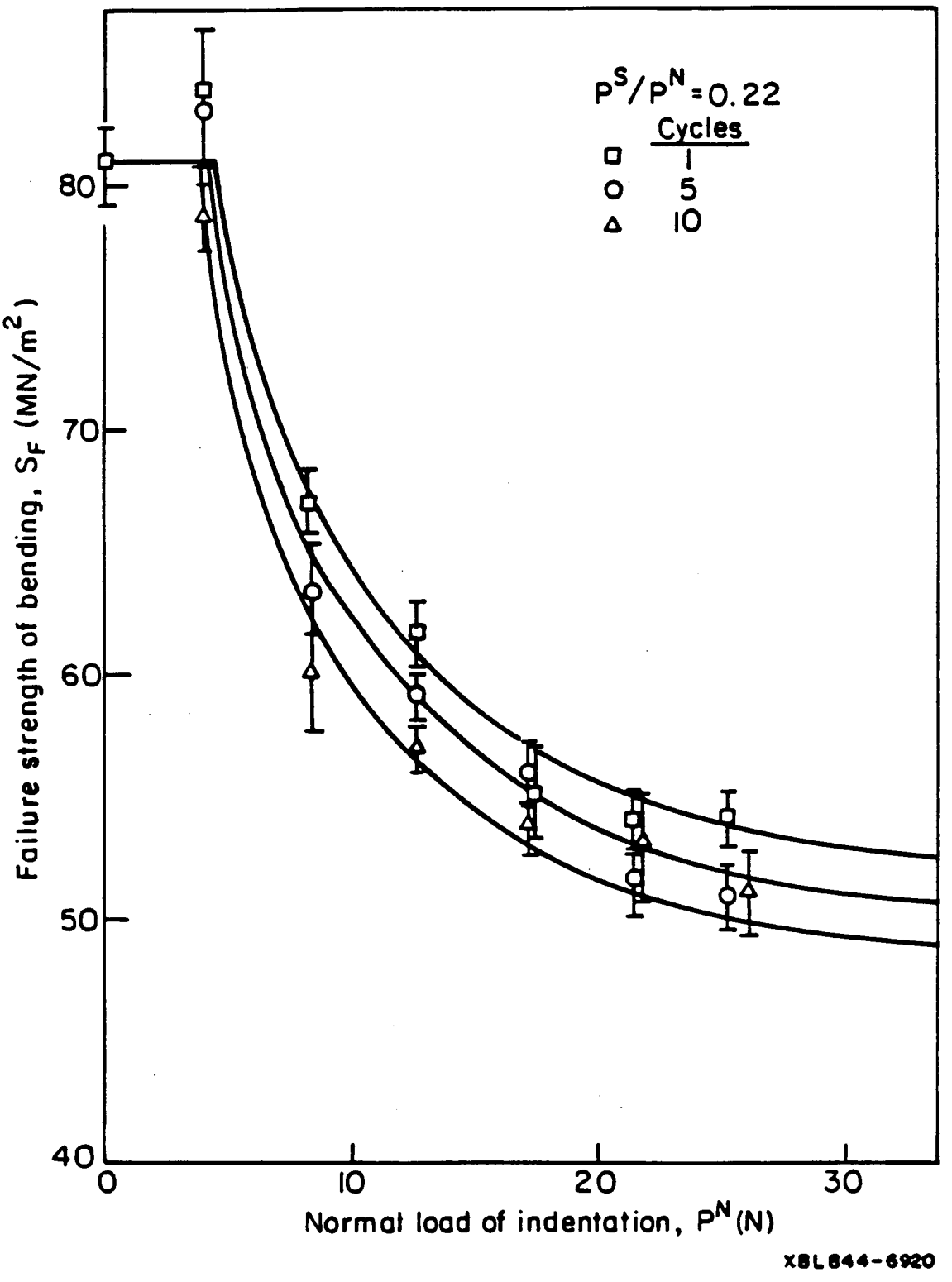
$P^S/P^N = 0.22$
Cycles
1
5
10
Failure strength of bending, S_F (MN/m^2)
80
70
60
50
40
0
10
20
30
Normal load of indentation, P^N(N)
XBL844-6920

Figure 18(a)

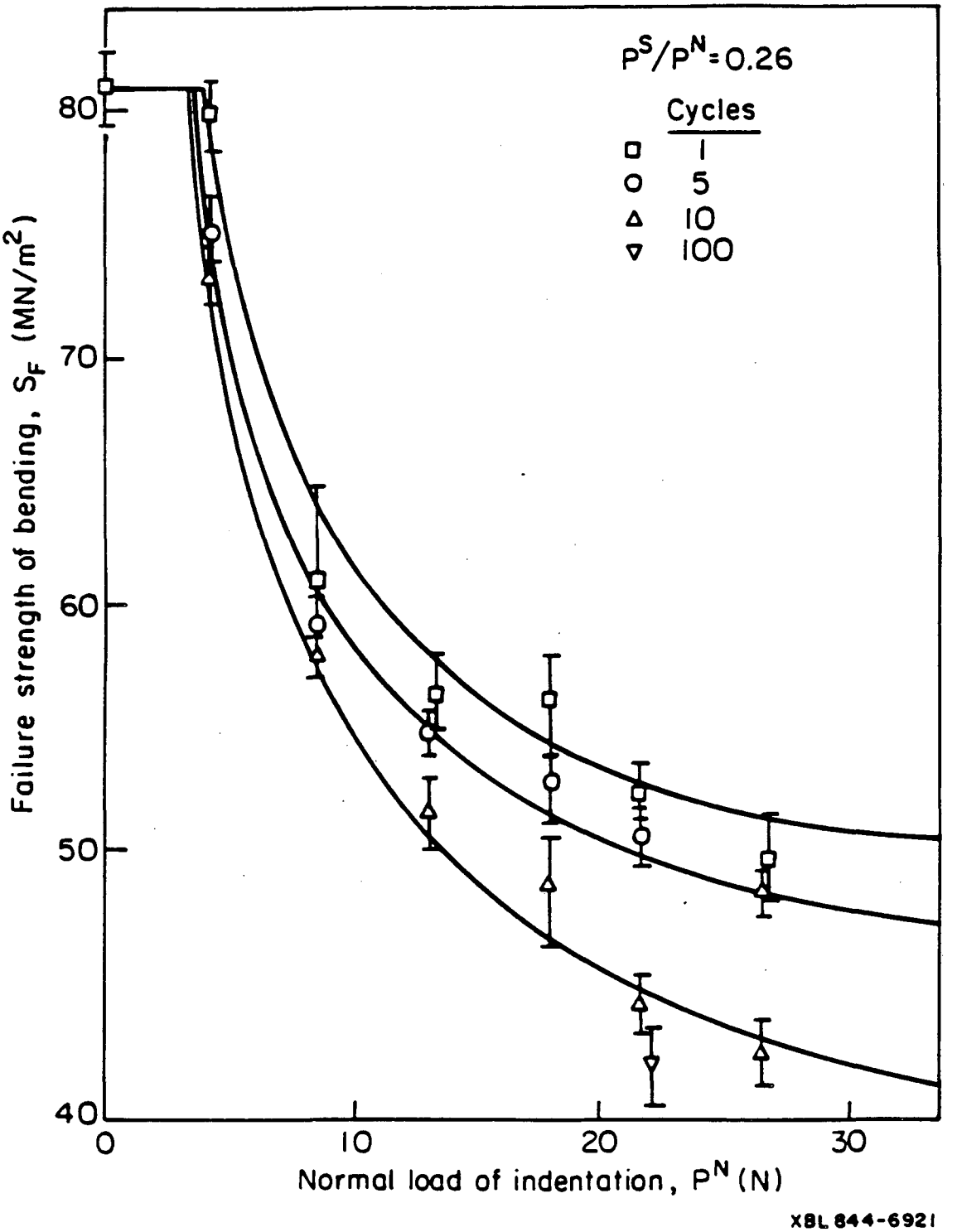
$P^S/P^N = 0.26$
Cycles
1
5
10
100
Failure strength of bending, S_F (MN/m^2)
80
70
60
50
40
0
10
20
30
Normal load of indentation, P^N (N)
XBL 844-6921

Figure 18(b)

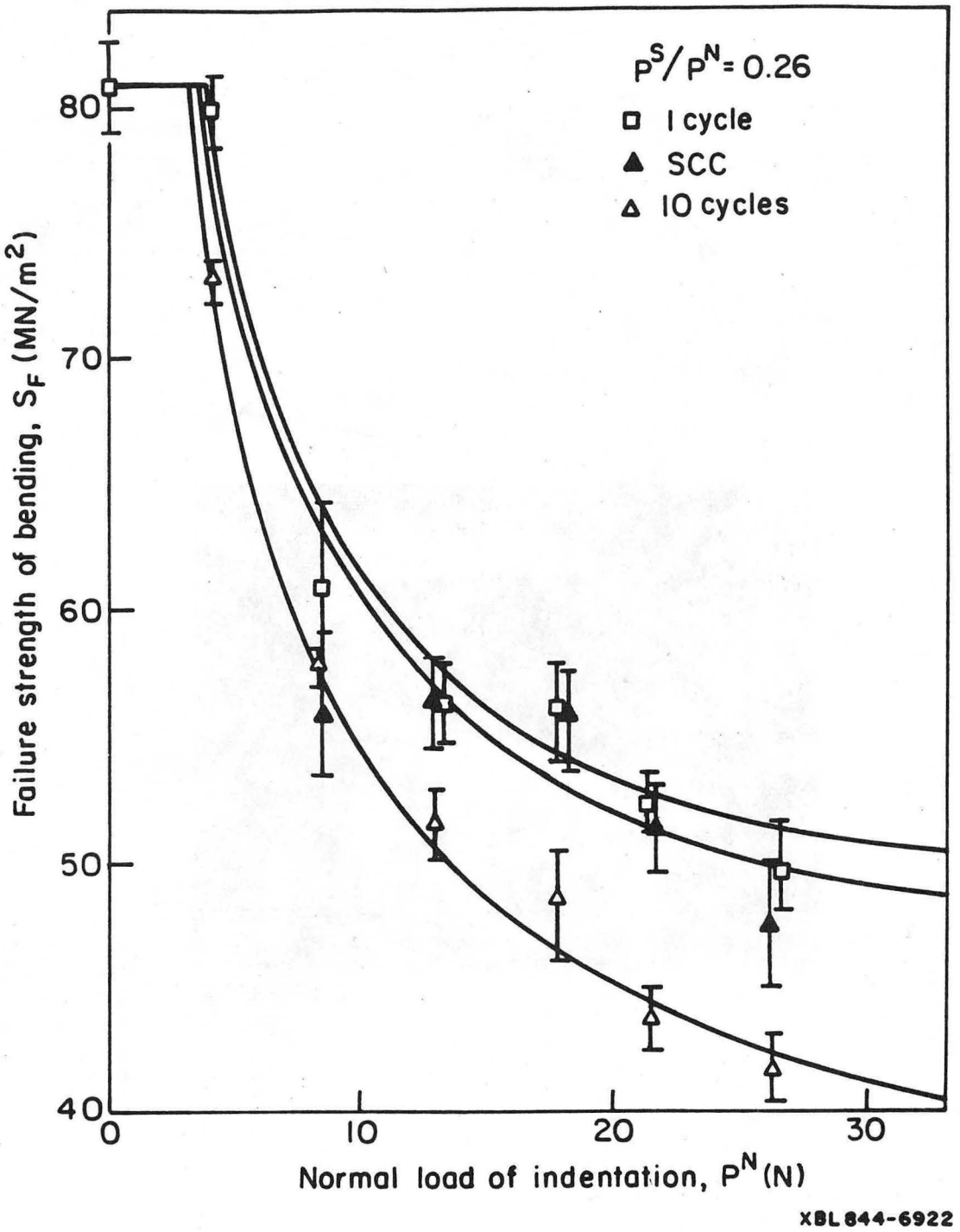
$P^S/P^N = 0.26$
1 cycle
SCC
10 cycles
Failure strength of bending, S_F (MN/m^2)
80
70
60
50
40
0
10
20
30
Normal load of indentation, P^N (N)
XBL 844-6922

Figure 19

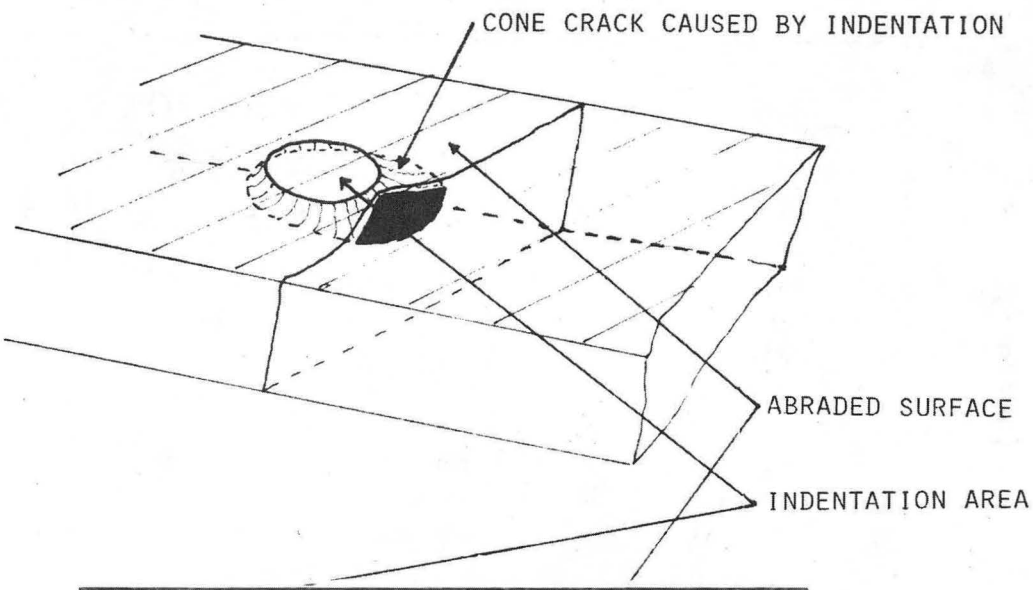

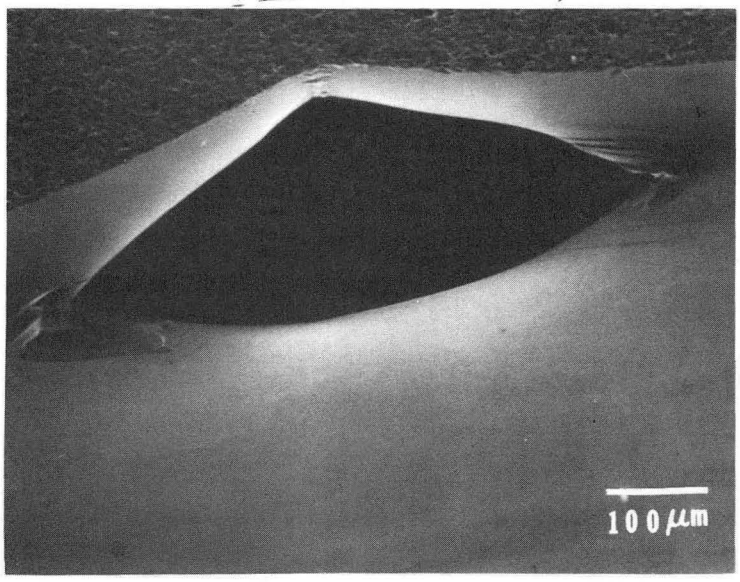

XBB 839-8246A

Figure 20

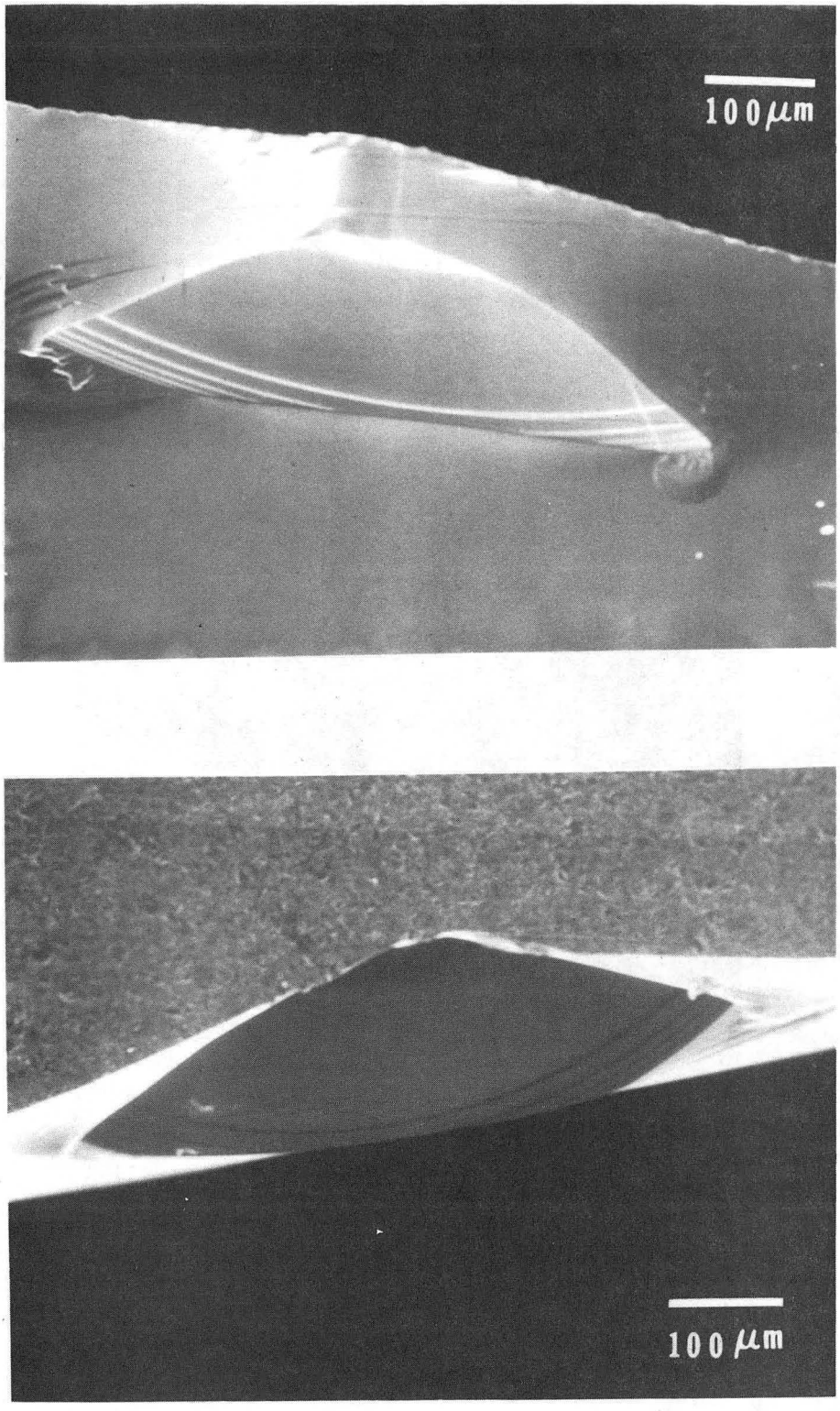

XBB 839-8247

Figure 21

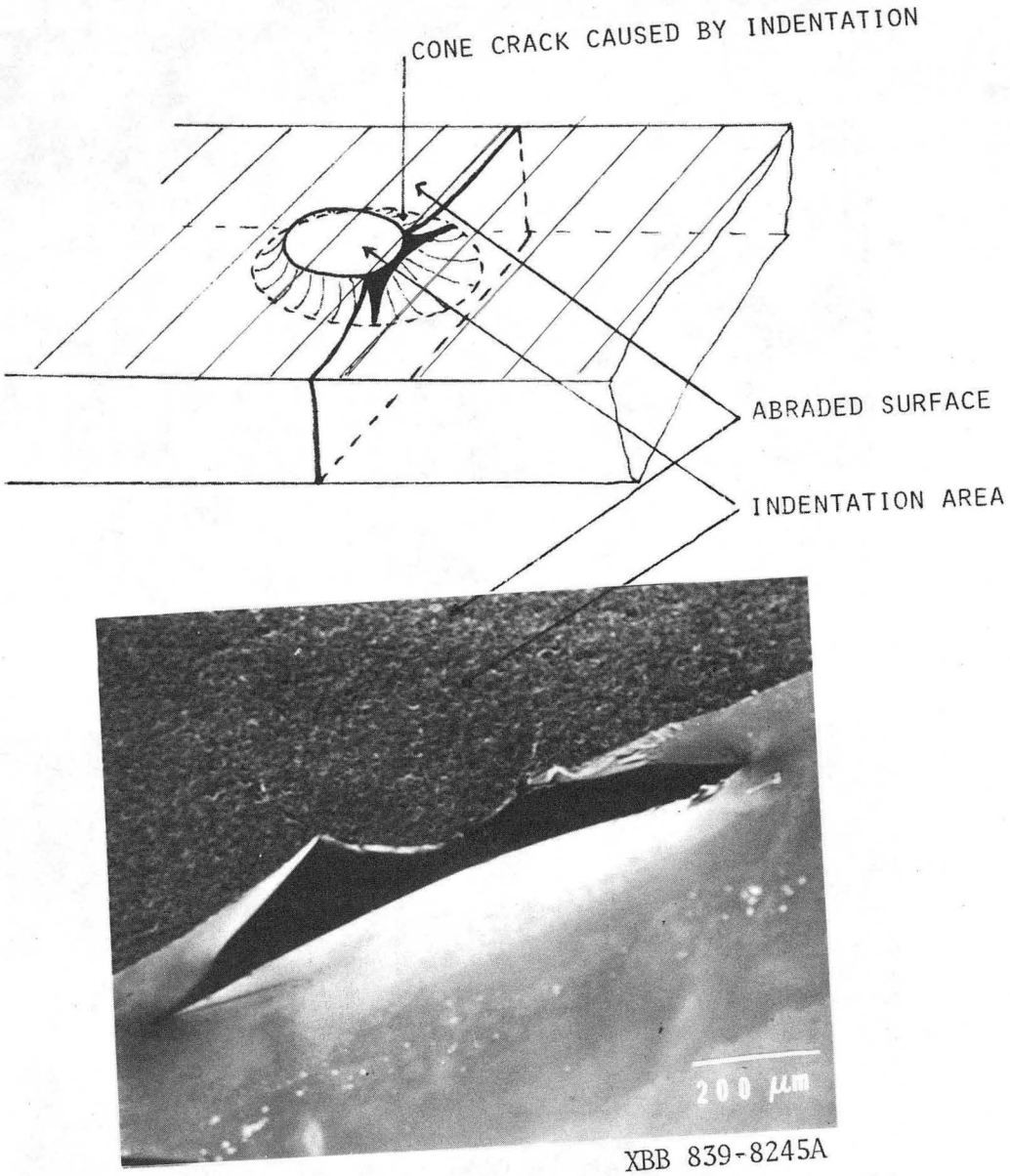
CONE CRACK CAUSED BY INDENTATION
ABRADED SURFACE
INDENTATION AREA
200 μm
XBB 839-8245A

Figure 22

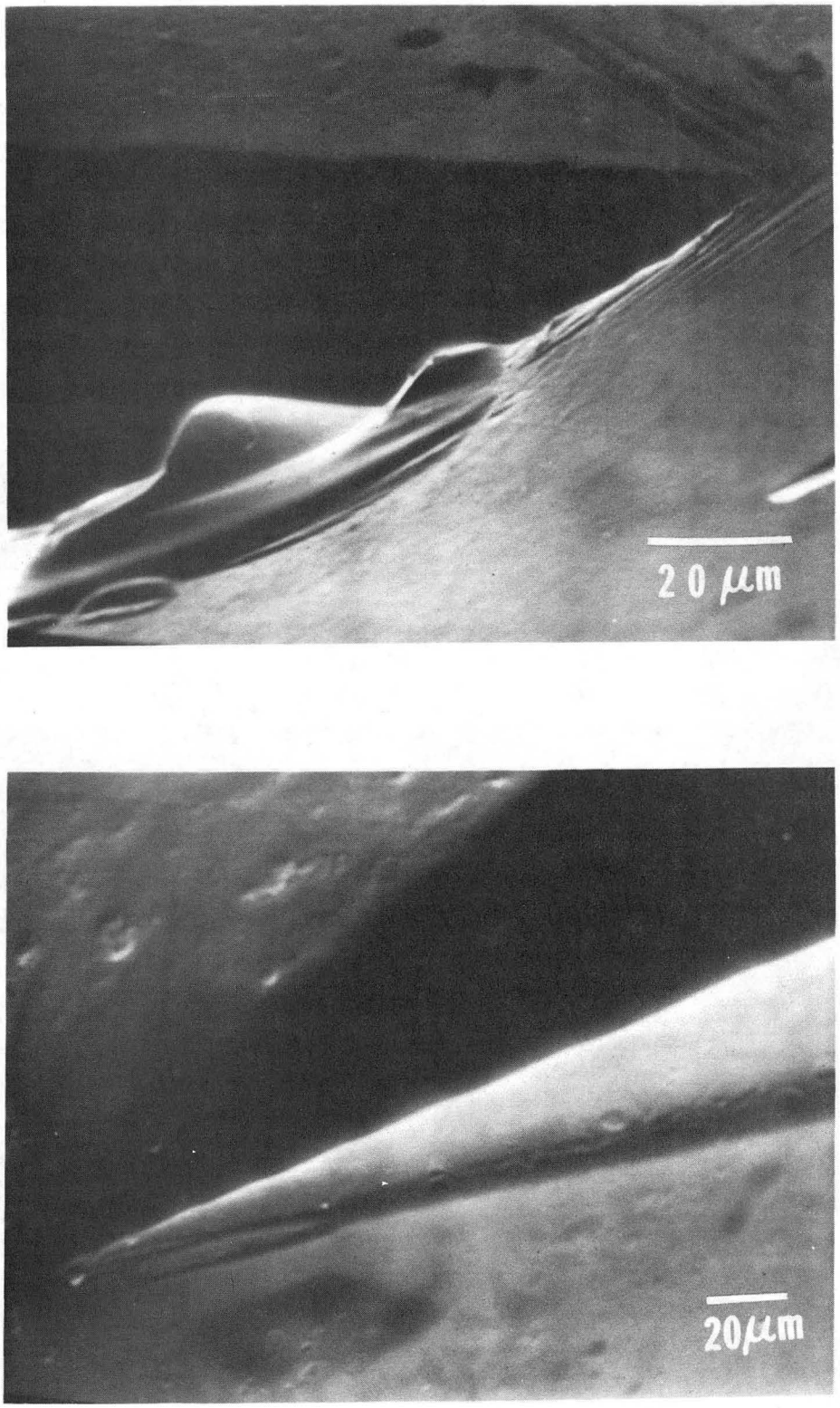

XBB 839-8249

Figure 23

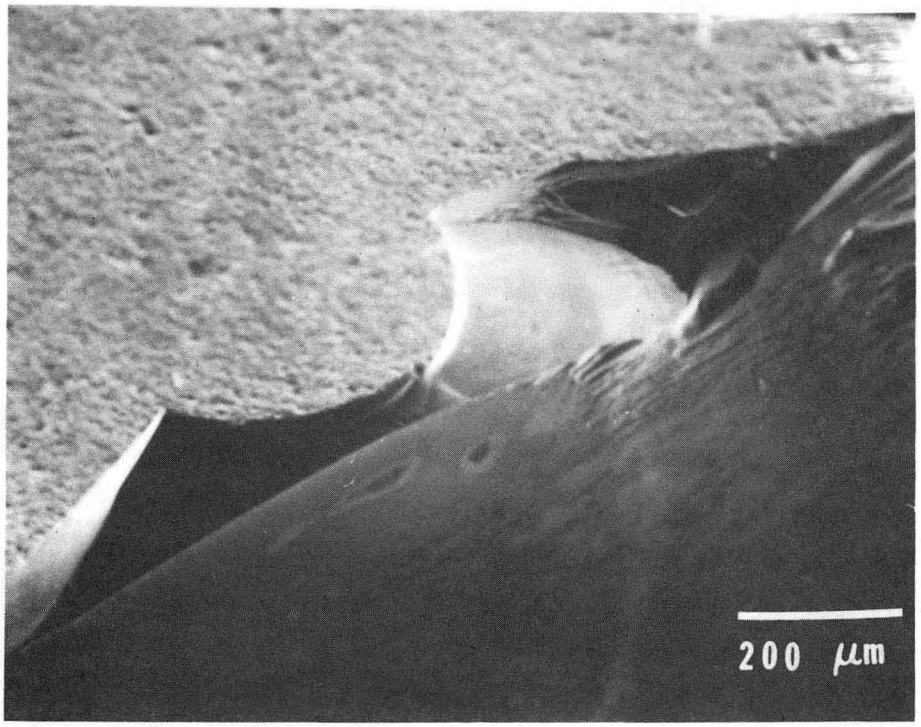

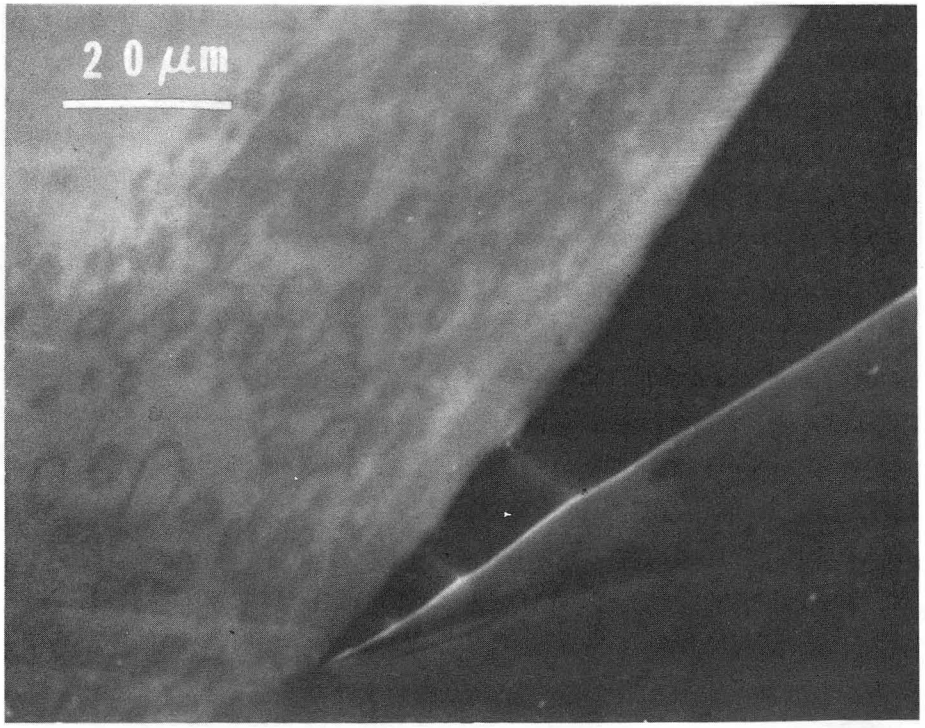

XBB 839-8248

Figure 24

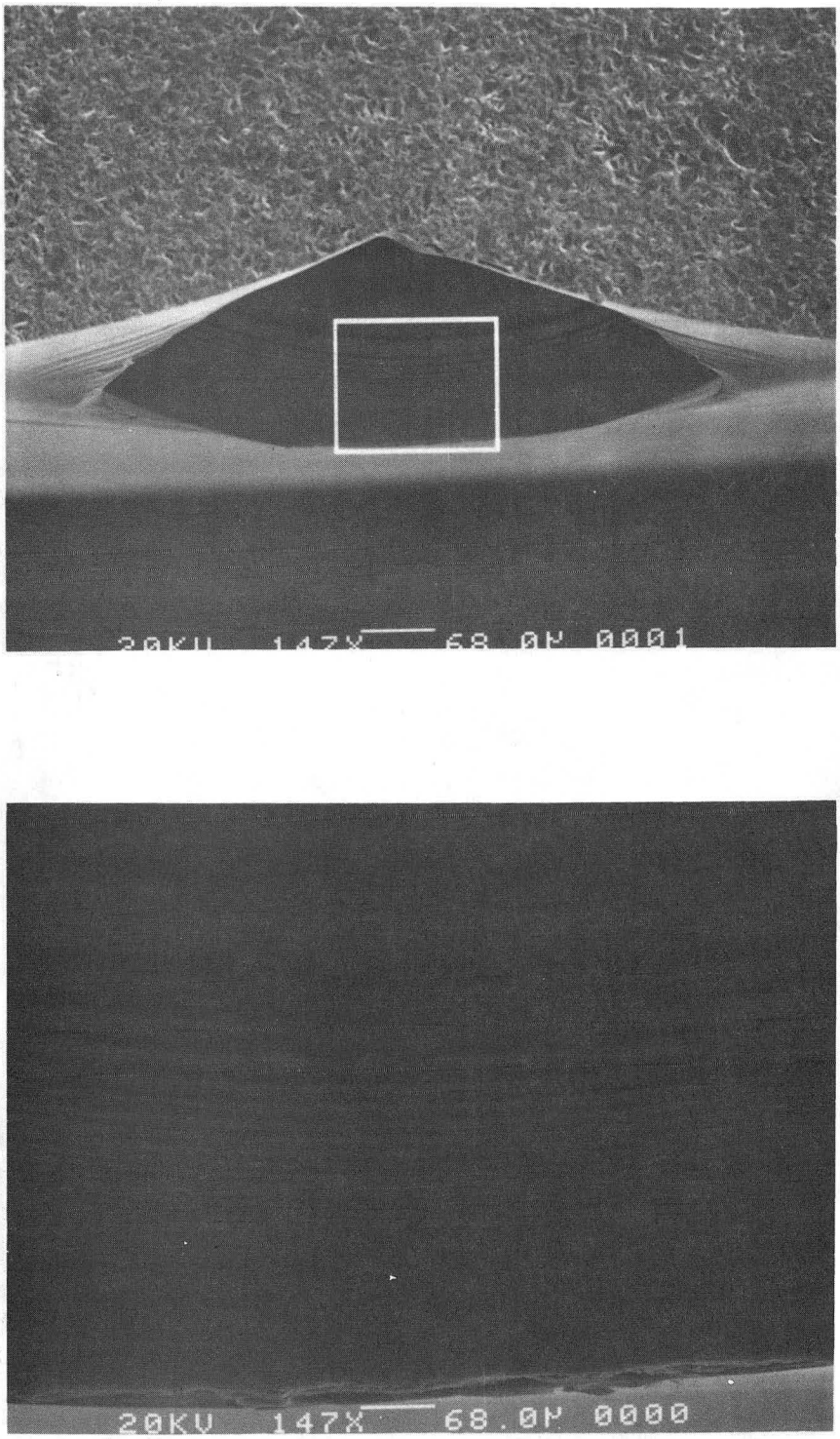

XBB 842-1233

Figure 25

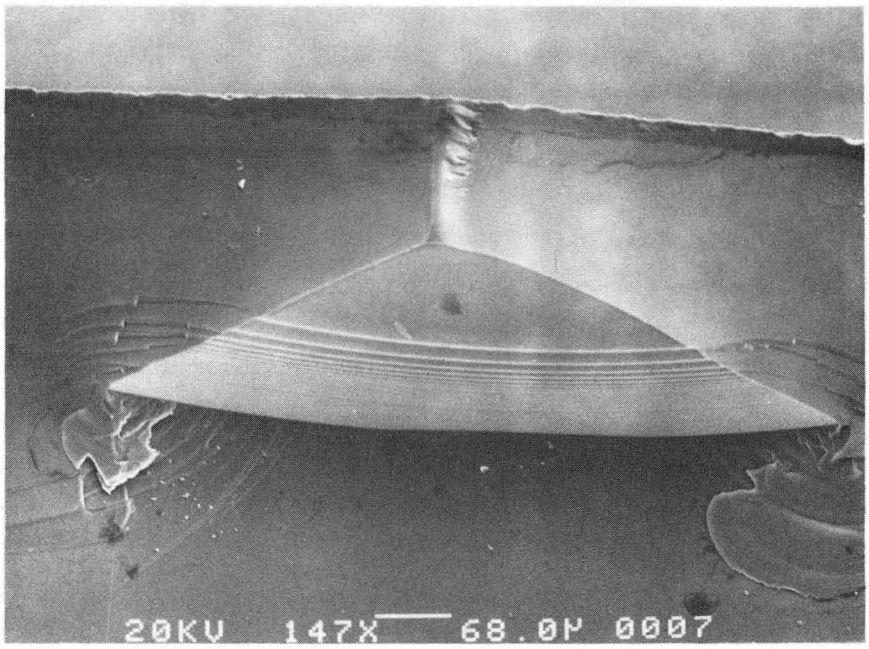

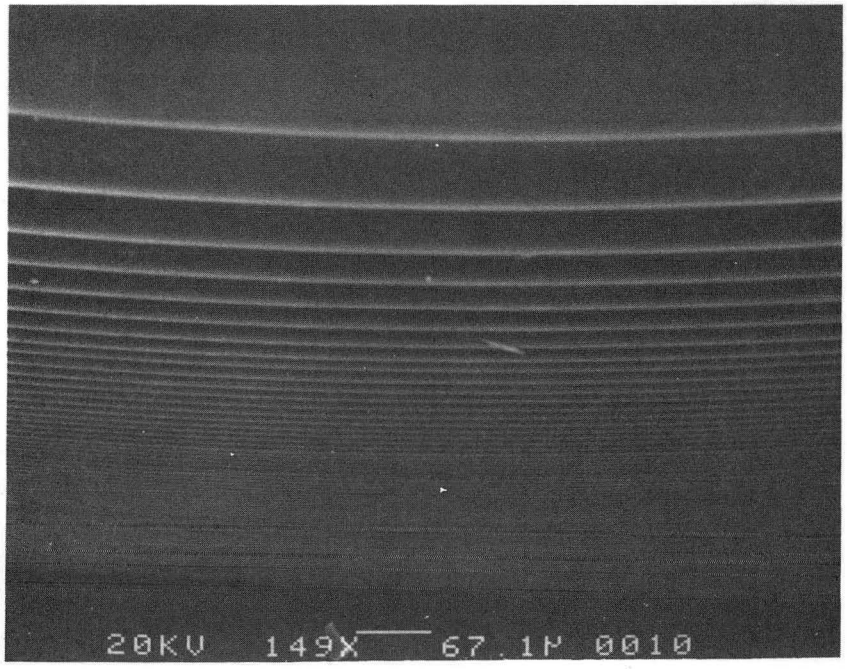

XBB 842-1232

Figure 26

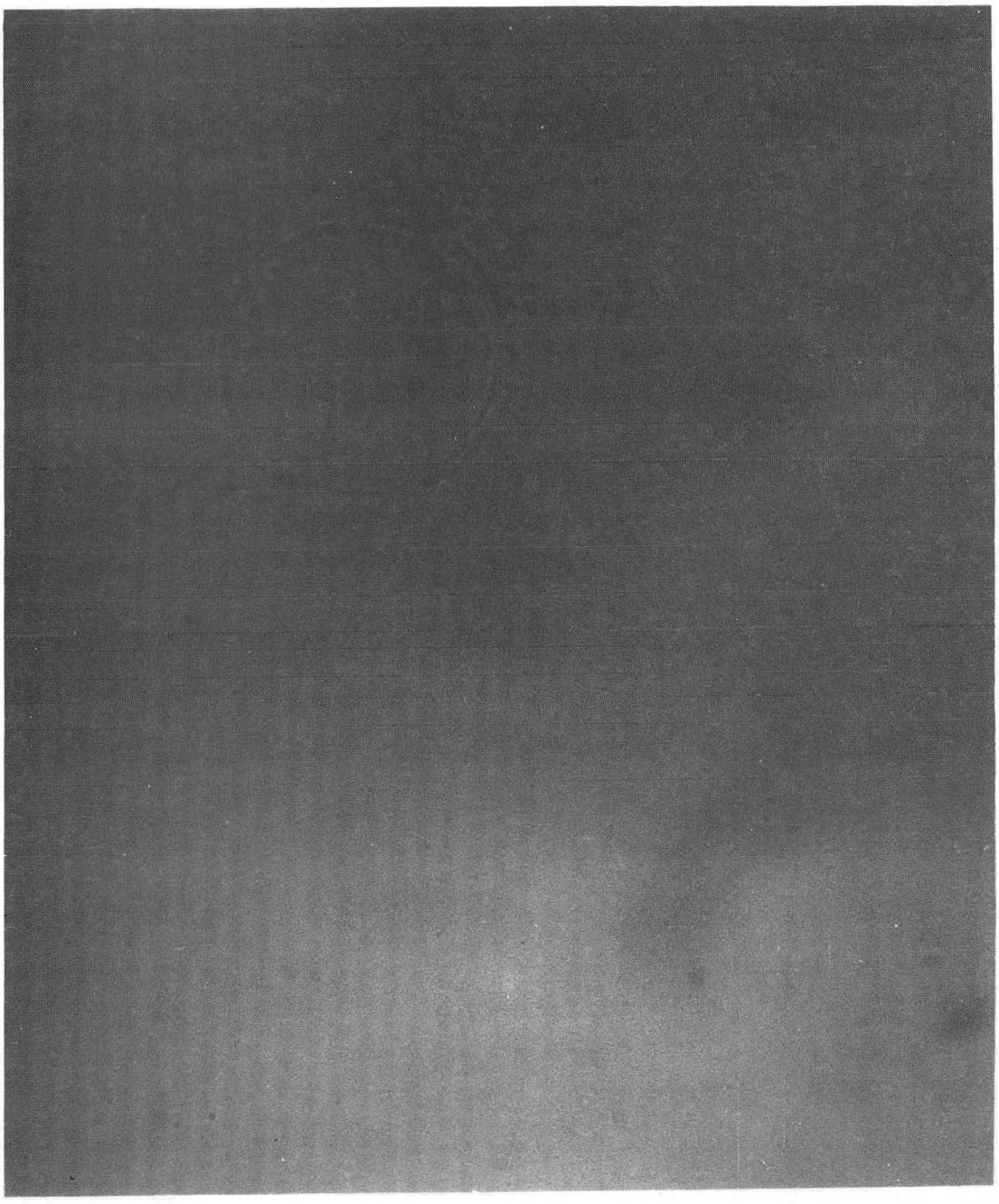

XBB 842-1231

Figure 27

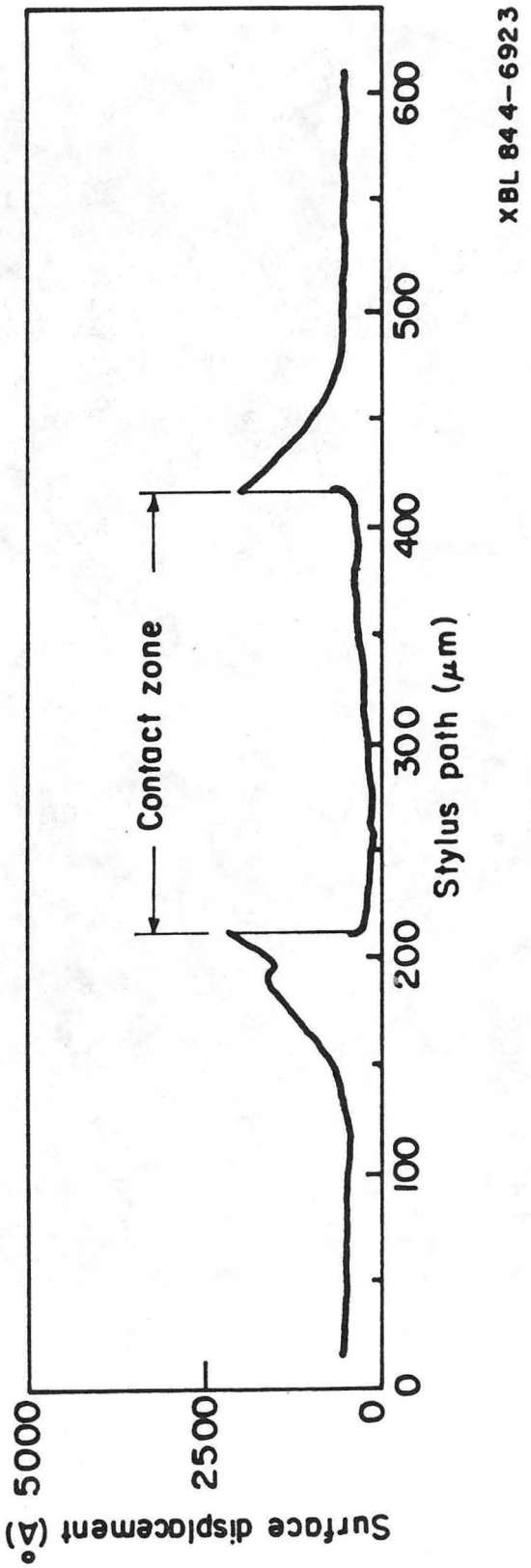
Surface displacement (Å)
5000
2500
0
0
100
200
300
400
500
600
Stylus path (μm)
Contact zone
XBL 844-6923

Figure 28

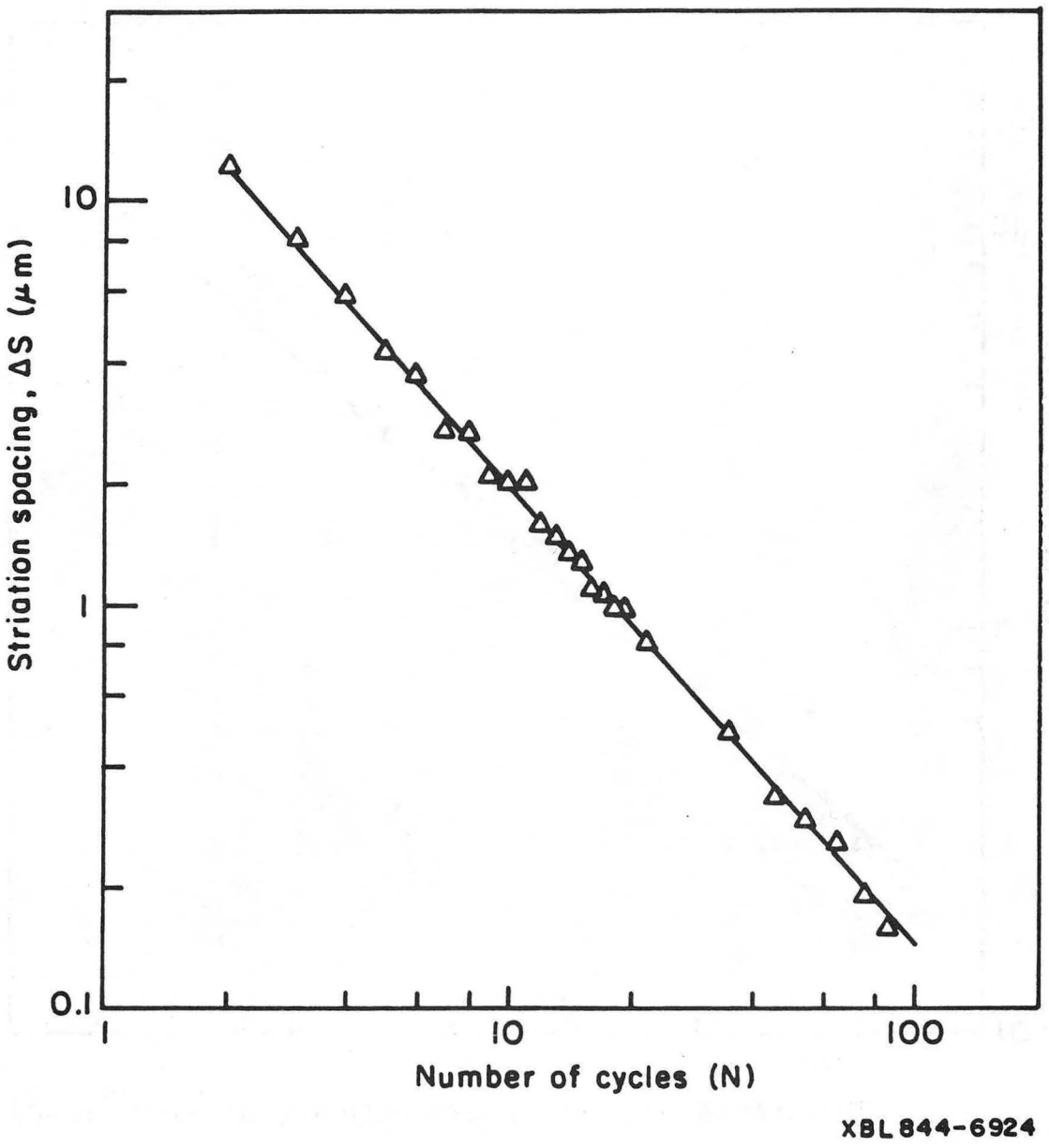
Striation spacing, ΔS (μm)
10
1
0.1
1
10
100
Number of cycles (N)
XBL844-6924

Figure 29

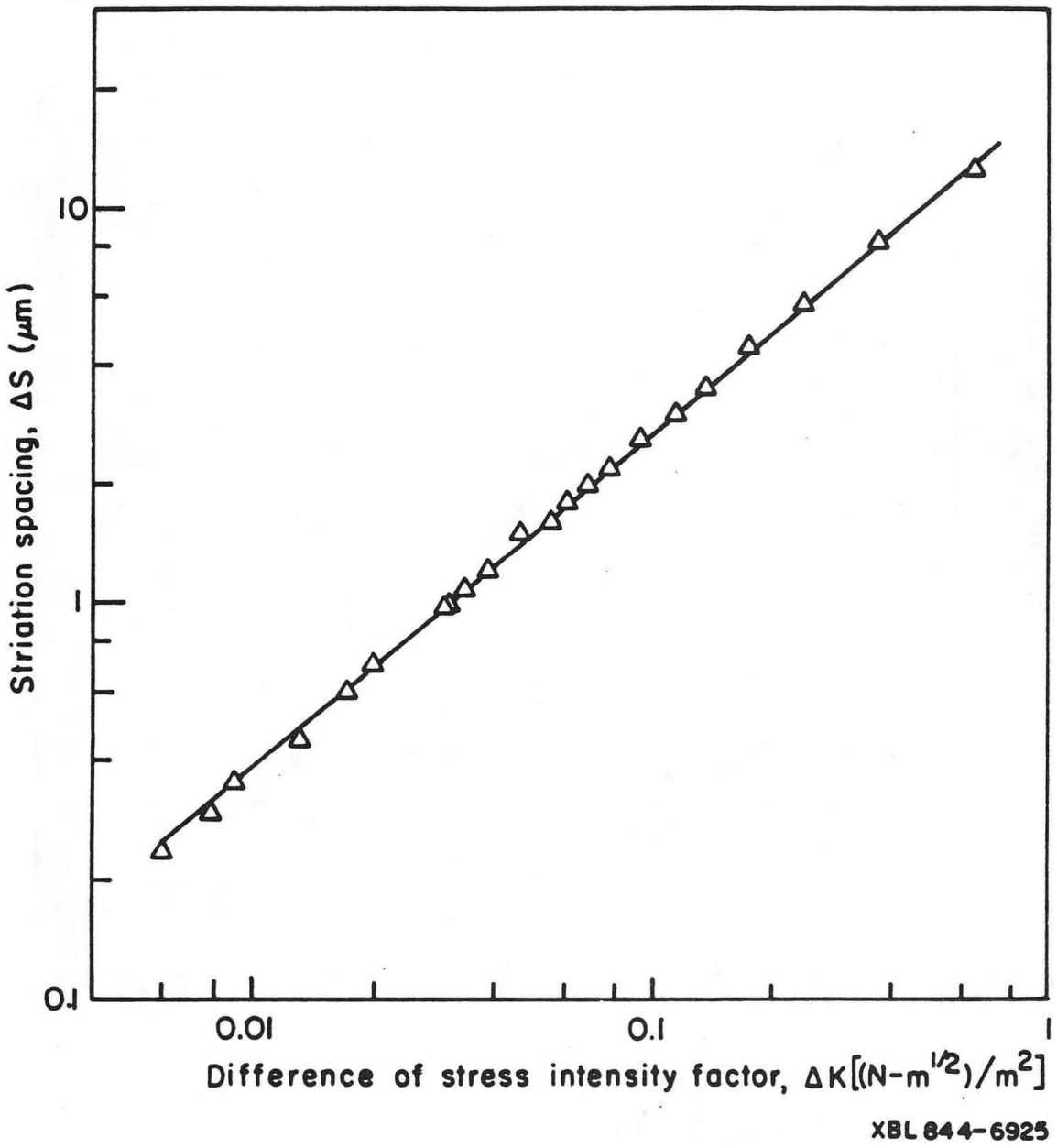
Striation spacing, ΔS (μm)
10
1
0.1
0.01
0.1
1
Difference of stress intensity factor, ΔK[(N-m^1/2)/m^2]
XBL 844-6925

Figure 30

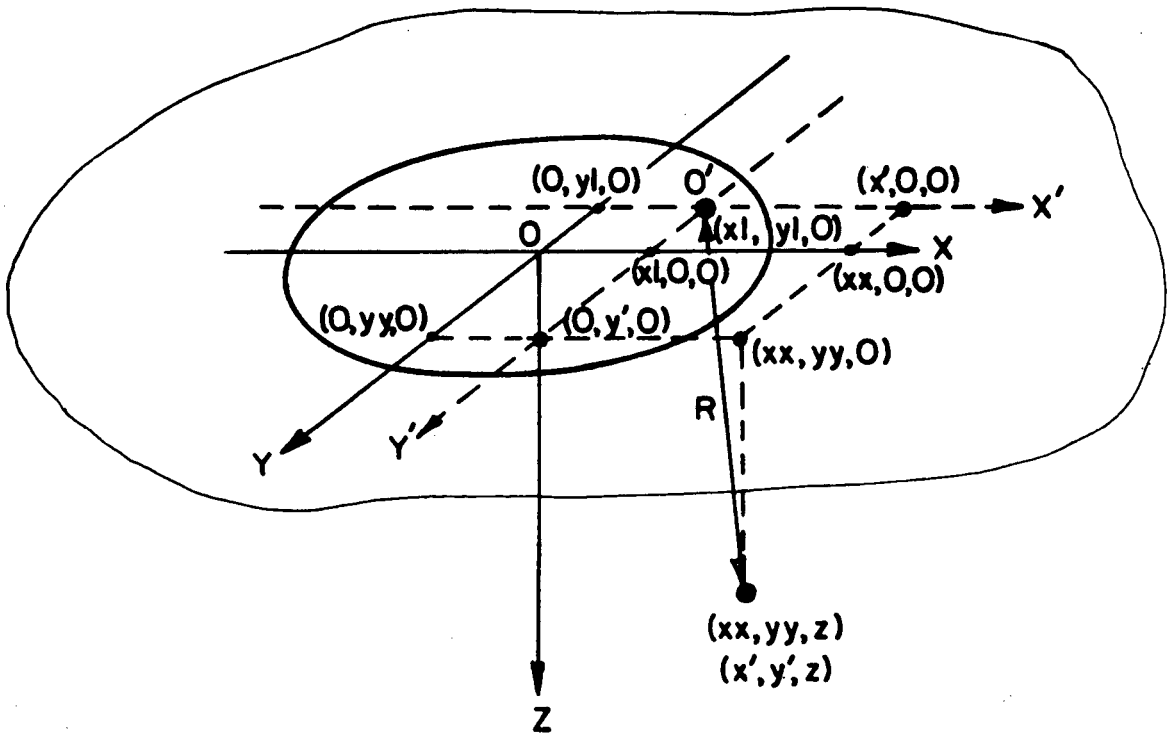
(0, yl, 0)
O'
(x', 0, 0)
X'
O
(xl, yl, 0)
X
(xl, 0, 0)
(xx, 0, 0)
(0, yy, 0)
(0, y', 0)
(xx, yy, 0)
R
Y
Y'
Z
(xx, yy, z)
(x', y', z)
XBL 844-6926

Figure 31

TECHNICAL INFORMATION DEPARTMENT
LAWRENCE BERKELEY LABORATORY
UNIVERSITY OF CALIFORNIA
BERKELEY, CALIFORNIA 94720